UNIVERSITY OF OSLO
Department of Informatics

Analysis of time variations of cardiac ultrasound image sequences.

Jacob Norenberg

August 29, 2013

Abstract

In today's medicine the use of ECG to capture the electrical impulses in the heart is widely used for detection of heart diseases, heart rates and also in imaging modalities to align images for 3D representation. The well-known ECG curve displays the electrical activity in the heart. In this thesis we wanted to find a new non-invasive supplement, or alternative curve, that displays the mechanical movements of the heart. This curve will hopefully include some of the same features as the ECG curve. This was done by only looking at the pixel intensities throughout an ultrasound recording of the heart, and capturing the mechanical movements. The motivation was based on an article written by Aase et al. An approach of using the histogram-based methods such as entropy, mutual information and earthmovers distance where first tested, but did not lead to any good results. The two dense optical flow algorithms by Lucas & Kanade and Färneback were then tested on the ultrasound recordings. By calculating the mean and variance of the length and angels of the flow vectors it was possible to create curves indicating the heart movements. These curves, and especially the angular variance of the flow vectors, contained features that can be associated with events in the heart. The curves seem to be characteristic for at least apical ultrasound scans of healthy volunteers, and independent of heart rate and subject.

Acknowledgments

Then I have come to the end of my studies here at the University of Oslo. It has been some very educational years. Going from a field where I was one of the best, to a field where I have felt like a newbie, has been challenging. I have learned so much new and met so many interesting people the past 2,5 years. I will start to thank Andreas Austeng, to be honest; I would not have completed this study if it had not been for you. You have guided me through the studies and also been an excellent co-supervisor for my thesis. I would also like to thank Eigil Samseth at GE-Vingmed for providing me with an interesting thesis and being my main supervisor.
Thank you, all helpful, smart and interesting professors, PhD students and students in the DSP group at the 4th floor of the Informatics building. You have always said yes and been very assistant when I have been asking for an advice. A special thanks to professor Fritz Albregtsen, PhD student Knut Landmark and Miss Moen for reading through and giving me feedback during my work.

List of Figures

List of Tables

Contents

Chapter 1

Introduction

1.1 Motivation for the project

In medicine today a lot of scientific research is done on the basis of the electrocardiogram (ECG). The ECG is a recording of the electrical activity in the heart, recorded from selected points on the surface of the body. The electrocardiogram can be considered a signature of the heart's electrically induced movements. An illustration of the ECG curve of a healthy heart is shown in Figure 1.1. The ECG is the most commonly used tool for diagnosing heart diseases, but it is also used as a reference in many new modern imaging modalities. Examples of this are stitching images together to create a 3D-image, displaying a cardiac cycle and finding the heart rate. Downsides with the ECG is that it is a separate measure where one has to put electrodes on the surface of the body and that it is only the electrical impulses of the heart, and not the mechanical movement, that it is measured. ECG can also be unstable and not give a useable result when used on people with certain heart diseases. Our main research question is: Would it be possible to find a novel and robust method to detect the heart's movement, in the form of a "mechanical" curve of a cardiac cycle, by only looking at the pixels in an ultrasound scan? Ultrasound scan is a low cost, easy and harmless acquisition modality that could be used for this purpose. An ultrasound acquisition of a cardiac cycle can be interpreted as a film consisting of many frames. Each frame is built up by pixels with gray level values or RGB values in the range between $0 - 255$.

1.2 Understanding and exploration

In the article *Electrocardiogram without electrocardiography* written by Aase [Aase et al., 2011] a method which uses the mean pixel intensity value of each frame to detect the cardiac cycle length was introduced. This article was therefore a good starting point for this project. To lay a good foundation for

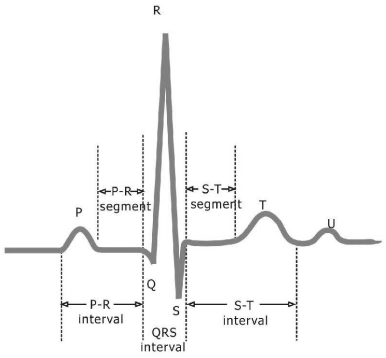

Figure 1.1: *The ECG signature of the heart.*

extending Aases cardiac cycle length estimation algorithm, the first task of this project was to reconstruct the first part of Aases algorithm and examine it to better understand its limitations. Sum of absolute difference was used as the similarity measure. With a signal processing background, the classical method, correlation, will also be tested out as an similarity measure. An extension of Aases algorithm would aim to remove some of the restrictions made; the minimum and maximum heart rate, which are commented on in his article.

1.3 Finding mechanical heart curve

As mentioned the main goal was to find a mechanical curve of the heart movement and movements in the heart that was "equal" for different subjects and heart rates, just based on the changes in gray levels between subsequent frames. Aases mean pixel intensity curve was therefore used as motivation and inspiration in the attempt to find a novel mechanical heart signature. In the initial description of this thesis, histogram-based methods such as entropy, mutual information and earth movers distance were set to be the approaches to be used. These approaches either use the information in one frame or the relation between two subsequent frames to try to find similarities. When the results from the histogram-based methods did not lead us to the desired result, the project left room for other methods to be tested, such as optical flow. Here a limitation of only using Lucas & Kanades and Färnebacks dense optical flow algorithms was set. If the results from the optical flow curve showed some interesting features, we would see if we could link those features to events from the heart movement, movements within the heart, the ECG curve or signs of potential heart diseases. This could then be helpful to use as an addition to the tools already existing in medical science.

1.4 Main contributions

There were two main contributions in this project. The first was the suggestion of making Aases cardiac cycle length algorithm independent of heart rate and testing Aases algorithm for different parameters.
The second and biggest contribution was the new angular variance curve created by using optical flow between subsequent frames, and the features in the curve that made it possible to see events occurring during a heart cycle.

1.5 Thesis outline

The thesis are build up by first introducing some background material and theory. Then the thesis are split into two parts because the project consist of two separate methods. The results and are discussed as they are presented. This to make it easier to understand why further choices was made. The two parts are combined with a general discussion and conclusion.

Chapter 2

Background and Theory

To get a better understanding of this thesis, some important theory and background are introduced in this first chapter. The chapter starts by introducing medical ultrasound and a few important aspects, such as resolution, speckle, cluttering etc. Then an introduction to the hearts anatomy, conduction system, physiology and different heart diseases is given. How the blood pressure changes in the heart and the basics of ECG will also be explained. The last part of the chapter has a more mathematical aspect. Here the two different similarity measures; Sum of Absolute Difference (SAD) and correlation are explained. The similarity analyzing tools Entropy, Mutual Information and Earth Movers Distance are presented, and at the end the computer vision tool optical flow is introduced with two different methods; the Lucas & Kanade and Farnebäck optical flow algorithms.

2.1 Ultrasound Imaging

Medical ultrasound imaging is a noninvasive technique used for gynecology, cardiology and cancer surveys, but maybe most know for baby scans. The acquisition is done by holding a probe to the skin surface and projecting an image of what is inside the body on a monitor. During World War I a principle for submarine detection was developed, called the sonar principle. Sonar is a abbreviation for **SO**und **NA**viation and **R**anging. The principle consist of transmitting a sound pulse and then wait for an echo of the transmitted pulse to return. This pulse is in the direction of an object of interest. If the velocity c, of the sound in the medium is known and t is the time from when the pulse wave was transmitted to the echo returns, the distance d to the structure can be found by

$$d = \frac{ct}{2}, \tag{2.1}$$

where the factor 2 is used because the pulse has to travel back and forth. This same principle applies for ultrasound imaging [Pope, 1999]. An ultrasound

beam is directed into the body from a transducer. The body's echo or reflection containing information about locations from different body structures is then analyzed. The ultrasoundsignal is attenuated as it travels through the body. When it meets a boundary between two media some parts of the ultrasound wave can be reflected and some transmitted. The attenuation describes a reduction in intensity as it travels through a medium. There are

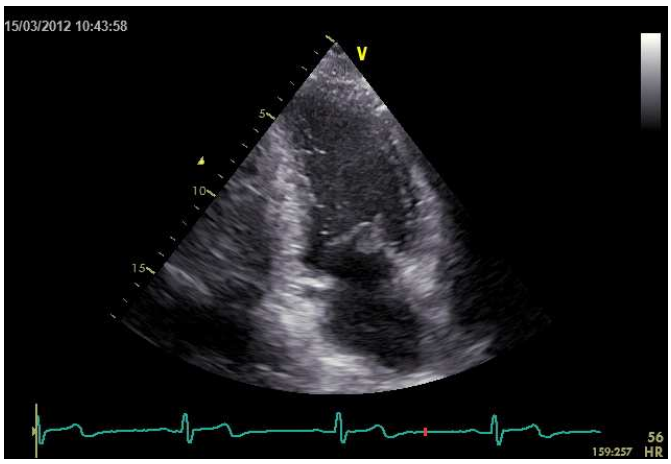

Figure 2.1: *Ultrasound image of the heart from GE-Vivid E9.*

several reasons for the reduction of intensity. The wave simply "spreads out" and suffers an "inverse square law" reduction in intensity, it may be scattered away from its original direction or it may be absorbed in the medium. It is the type of medium that decides the amount of absorption. Water has little absorption, and bone has high absorption of sound. Higher frequencies are affected by greater absorption, so if the frequency is doubled, the absorption increases by a factor of four [Pope, 1999]. This is a very important factor when choosing the best frequency for imaging the body. A high frequency may not be able to penetrate all regions that are supposed to be examined. The loss of the ultrasound wave intensity is measured on a logarithmic scale and the frequencies that normally are used in ultrasound imaging are between 1 and 15 MHz, but can also be higher [Pope, 1999]. Between two specific medias there is a specific acoustic impedance Z. The acoustic impedance is used to describe the opposition of a medium to the flow of sound waves. It describes how the sound wave 'adjusts' from one medium to another for efficient transmission. The specific acoustic impedance Z of a medium is given by

$$Z = \rho c, \tag{2.2}$$

where ρ is the density of the medium and c is the velocity of sound. Also notice that

$$Z_{gas} << Z_{liquid} < Z_{solid}.$$

If there is a big difference in the acoustic impedance Z between two media, the transmitted ultrasound wave can not easily adjust and most of the wave will be reflected as an echo. If the echo however is small between the two mediums, or said in another way, the acoustic match between the layer is good, a weak echo is reflected and most of the wave is transmitted [Pope, 1999]. The fraction of the intensity reflected back (I_r) to that incident (I_i), at a normal incidence, is known as the intensity reflection coefficient, α

$$\alpha = \frac{I_r}{I_i}, \tag{2.3}$$

which in turn is given by,

$$\alpha = \frac{(Z_2 - Z_1)^2}{(Z_2 + Z_1)^2}. \tag{2.4}$$

A large difference in Z gives a large α which implies strong echoes. This is one reason why ultrasound do not manage to give good imaging in parts of the body where there are a lot of bones or air, as in the lungs.

A-scan, or also called Amplitude scan, measures the range to the different layers. It records the time t it takes for the ultrasound pulse to travel to one medium and back. It estimates the depths or distances between the transitions of two different media [Pope, 1999]. The echoes received back from the different layers are converted to spikes arising from a baseline. The grater the difference in two media at each layer the higher the spike becomes. An A-scan gives a 1D image.

M-scan is the same as M-mode. It can be seen as A-scan over time, and was the first modality to record moving echoes from the heart. This is why the motion can be interpreted in terms of myocardial and valvular function. This is now used in context with B-scan [Stoylen, April 2013].

B-scan image, or also called Brightness imaging, is accomplished by illuminating the object by sweeping an ultrasonic beam of short time duration and recording the resulting echos. This is done in the same way as an A-scan. The difference is that for a given location of the ultrasonic transducer each echo is displayed as a bright spot at a position corresponding to its arrival time. A B-scan image is based on the changes in the acoustic impedance of the object and gives a 2D image as a function of time [Fatemi and Kak, 1980].

To have a good imaging of structures such as blood or the heart, the framerate plays an important role. It is important to have a high enough framerate to get a good imaging of the motion speed of an object. An eye can only see 25 frames per second, giving a temporal resolution of about 40 ms [Stoylen,

April 2013]. A typical 2D ultrasound image is made of a few tens of lines (64-512) [Pope, 1999]. The frame rate of the image is set by the time required to transmit a beam, receive and process the backscattered echoes from the medium, for all the lines of the image. For a conventional 2D image the time t_{image} to build an image is,

$$t_{image} = \frac{N * 2 * R_{max}}{c}, \tag{2.5}$$

where N is the number of lines in the image, R_{max} is the image depth and c the speed of ultrasound waves that is assumed constant (1540 m/s). The maximum frame rate is then given by,

$$FR_{max} = \frac{1}{t_{image}}. \tag{2.6}$$

The framerate will therefore scale with the depth of field. A reduction will give a higher frame rate. This higher frame rate can be used for higher temporal resolution[1] or to increase the spatial resolution[2] by increasing the center frequency of the imaging pulse. This because the lateral resolution scales with frequency through the Rayleigh resolution [Johnson and Dudgeon, 1992]

$$\theta_R \approx \frac{\lambda}{D}, \tag{2.7}$$

where D is the aperture size, λ the wavelength and θ_R the angle, or sector width [Stoylen, April 2013].

2.1.1 Resolution

Good resolution is necessary when you want to see very small structures in an image. A typical ultrasound image is shown in Figure 2.1. Resolution is the description of "fineness of detail" in an image, so if an image has good resolution, small structures are easier to detect or distinguish. Lateral (along the axis of the beam/vertical) and axial (depth/horizontal) resolution is the two types of resolution that are considered. It is the description of how the beam manages to separate two objects at different distances. The shorter the pulse is, the better axial resolution you get [Pope, 1999]. This is given by the bandwidth. Lateral resolution describes detail distinguishable in the image plane at right angles to the beam. It depends on the width of the beam: Narrow beams give good resolution. As earlier described, high-frequency beams produce better lateral resolution because the aperture size D measured in wavelengths is larger and θ_R smaller, see Eq. (2.7). But high-frequency beams suffer from grater absorption. It is important to find

[1] Precision of a measurement with respect to time.

[2] The measure of how closely lines can be resolved in an image.

a compromise between resolution and penetration. For a given aperture D, this is controlled by the center frequency. The practical frequency is usually restricted to be between 1 and 15 MHz [Pope, 1999].

2.1.2 Speckle

The ultrasound image is usually degraded by coherent wave interference known as speckle. Speckle is a random deterministic interface pattern which shows up as small-scale brightness fluctuations in all parts of the image, and it is especially visible in homogeneous regions of tissue. The texture of the speckle pattern does not correspond to the underlying structure. The local brightness of the speckle pattern reflects the local echogenicity of the underlying scatters. Speckle is the sum of all small echo contributions.

2.1.3 Cluttering

In ultrasound imaging clutter is a noise artifact that appears as diffuse echoes overlying structures or the signal of interest. The easiest place to detect clutter is in anechoic[3] and hypo-echoic[4] regions, and it is seen in a wide range of imaging applications. Clutter often obscures targets of interest and complicates anatomical measurements [Lediju et al., 2008].

2.1.4 Image registration

In digital image processing it is often necessary to align images of the same scene that have been recorded at different times, from different perspectives or with different types of sensors. The objective of image alignment is to register the first (input) image against the second (reference) image, so that we can accurately compare the results from the different sources. In order to do this we have to determine the geometrical transformation function between the images that we wish to compare [Gonzalez and Woods, 2008]. There are several types of situations that require the use of image registration in order to align two or more images. When choosing a technique for image registration it is important to consider the known causes of image distortion in the type of application that is to be used [Brown, 1992]. There are different ways to classify and categorize the approaches used for image registration. Examples of these types of categories used in medical image registration mentioned in [Fitzpatrick et al., 2000] are; number of dimensions of the image spaces involved, registration basis, geometrical transformation, degree of interaction, optimization procedure, modalities, subject and object [Maintz and Viergever, 1998]. The category that is related to geometrical

[3] Regions which neither have or produce echoes.

[4] Giving off few echoes; said of tissue or structures that reflect relatively few of the ultrasound waves directed at them.

transformation represents the mathematical part of image registration where the goal is to align the points in one image with the same points in a different image. These points can either correspond to the same object, or a different object with the same "shape". An example of a type of modality is the intermodal registration we have when the images involved are from two different sensors. The degree of interaction simply refers to whether the registration algorithm is automatic or needs adjustments during the process. Throughout the registration process it is important to estimate the quality of the procedure by using a function that relates the images and the mapping between them together. This function is then optimized in some way that will give a high degree of accuracy. In the case of medical imaging the subject and object categories refers to the involvement of the patients, and the location and area being examined [Fitzpatrick et al., 2000].

2.1.5 Image stitching

Image stitching is the process of stitching together overlapping images with their overlapping fields. The process can be divided into three main components; image registration, calibration and blending. In ultrasound imaging ECG gated stitching of sub-volumes acquired from different cardiac cycles is a technique to increase the volume size, while maintaining the frame rate [Badano et al., 2011]. The technique gates over several cardiac cycles. ECG gated stitching is prone to motion artifacts caused by transducer moments, respiration and varying heart rate [Badano et al., 2011].

2.1.6 Compounding

Ultrasound compounding aims to improve image quality by averaging several coplanar ultrasound frames into a single image. In principle, compounding imaging starts by scanning frames from different view angles (frequencies or strain conditions), which produce different artifact patterns. Averaging these independent frames suppresses the artifact and reinforces real structures. However, the compound image can suffer from blurring due to misalignment between frames if the transducer or the target move too rapidly. This blurring effect causes a significant reduction in the sharpness of compound images, especially in ultrasound motion sequences [Lin et al., 2005].

2.1.7 Echo stress

Stress echocardiography is monitoring the heart under physical stress. A recording is taken under rest to find a baseline of the patients heart walls movements. Then the patient is put under physical stress forcing the heart rate to increase and new images are recorded. New observations of the heart

walls are done. Ischemia[5] of one or more coronary arteries could cause a wall motion that is abnormal and this could indicate coronary disease (CAD). This will be explained more in chapter 2.2.6. The ECG is used to monitor the heart.

2.2 The Heart

The main cause of death in Norway is cardiovascular diseases. There are around 15000 heart attacks and 5000 deaths of cardiac diseases in Norway each year [StatisticsNorway, 2011]. One method to detect heart diseases is using electro cardiogram (ECG). ECG is a graphical recording of electrical signals generated by the heart. Pacemaker cells generate electrical impulses that lead to a depolarization of the cardiac muscle. The depolarization and repolarization of the cardiac muscle generate the electrical signal presented as an ECG curve. The physiological base of the depolarization is caused by action potential in the cells. The cells are normally negative loaded compared to the surrounding tissue fluid. It is the pacemaker cells impulse frequency that is responsible for the heart rate in a normal heart. The ECG can therefore in a way be interpreted as the electrical signature of the heart. The ECG and the hearts mechanical movement are not fully coherent[6]. As mentioned in the introduction, one of the goals for this master project is therefore to find a different method than the ECG to measure the hearts movements by using the information from the pixels in the ultrasound images. In our analysis we will use ultrasound acquisitions of both an apical four-chamber view and an apical long axis view (apical three-chamber) as illustrated in Figure 2.3. To get a better understanding of what we see in the ultrasound pictures, a brief introduction to the hearts anatomy, conduction system and the heart muscular physiology are given in this section. Also some heart diseases that are related to ultrasound imaging is mentioned. The description and interpretation of the Echo cardiography will also be described. This will give a better foundation when the ECG later will be used as a referace.

2.2.1 Anatomy of the heart in adult humans

Figure 2.2 displays the anatomy of the heart. The heart is a blood pump built up by heart muscle cells. The heart muscle is different from the skeletal muscles and smooth muscles. The heart consists of four chambers as seen in Figure 2.2; the right atrium, the right ventricle, the left atrium and the left ventricle. The superior vena cava and inferior vena cava lead the blood

[5] Lack of sufficient oxygen supply.

[6] A property holding for two or more waves or fields when each individual wave or field is in phase with every other one.

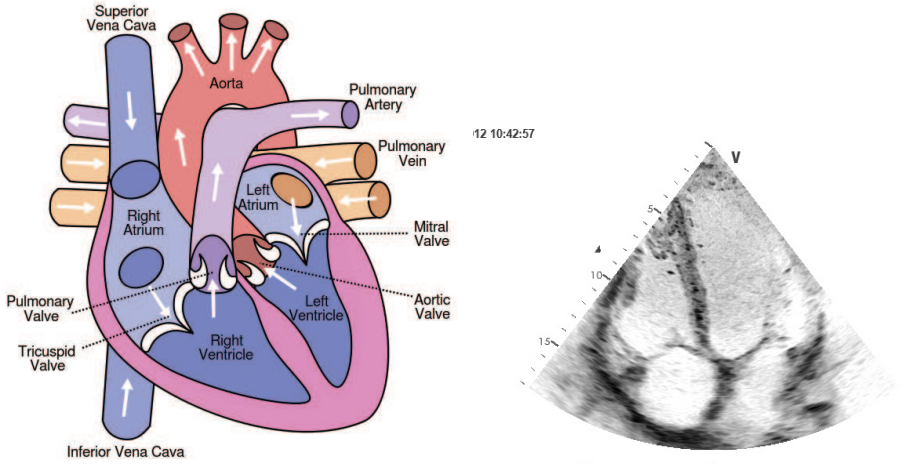

Figure 2.2: *Left: Illustration of the hearts anatomy [Wikipedia, 2013a]. Right: An apical four-chamber ultrasound scan.*

from the body into the right atrium. Between the right atrium and the right ventricle you find the tricuspid valve. The tricuspid valve has tree leaflets and they are connected to the papillary muscle in the right ventricle. From the right ventricle the blood floods through the pulmonary valve into the pulmonary artery. The pulmonary valve also has tree leaflets. The blood returns from the lungs through the pulmonary into the left atrium. The mitral valve is between the left atrium and the left ventricle. The mitral valve is bicuspid[7], and it consists of two leaflets connected to papillary muscles in the left ventricle. The wall between the left and right ventricle is called the septum interventriculis and the wall between the left and right atrium is called the septum interatrialis. The wall around the left ventricle is thicker than the wall around the right ventricle. This is because the blood leaves the left ventricle through the aortic valve out into the whole body and therefore needs more power to be "shipped" out. This caused by a higher pressure in the systemic circulation. A sack called pericardium surrounds the heart. The chambers are covered with endothelium, a type of cells that prevents the blood from sticking to the walls. In Figure 2.2 the mitral, tricuspid and aortic valve are displayed. These are the valves that are used as a reference to make sure the correct ultrasound acquisition is performed when recording an apical long axis scan or an apical four-chamber scan. The left image in Figure 2.3 presents an apical long axis scan where the mitral valve are to the left and the aortic valve is to the right. The figure to the right presents an apical four-chamber scan where the tricuspid valve is to the left and the mitral valve to the right.

[7]Having two point or cusps.

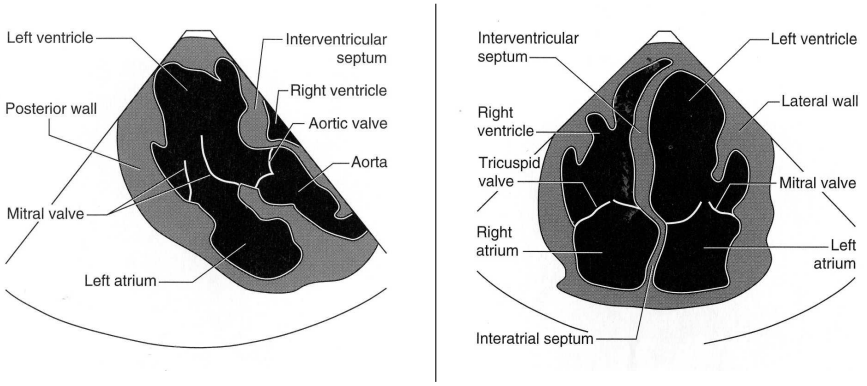

Figure 2.3: *The left figure shows how an apical long axis scan should look. Both the mitral valve and the aorta valve should be visible. The right figure shows an apical four-chamber scan. Both the tricuspid valve and the mitral valve should be visible [Tempkin and Leonhardt, 2009].*

2.2.2 The heart conduction system

The heart is innervated by the sympathetic and parasympathetic nerve system as seen in Figure 2.4. The sympathetic nerve system makes the heart beat faster, the parasympathetic makes the hearth beat slower. The nerves influence the sinoatrial (SA) node situated in the right atrium. The SA node normally decides the heart rate and this is normally the pacemaker of the hearth. The depolarization of the SA node triggers the depolarization of the atrial walls leading to the depolarization of the atrioventricular (AV) node that is placed in the bottom of the right atrium. After depolarization of the AV node the depolarization is conducted through the "bundle of His", also called the AV-bundle of His, located in the septum and spread through the walls of the ventricles causing a depolarization of the ventricle walls. The depolarization lead to a contraction of the ventricles.

2.2.3 Heart muscle physiology

The right and left atrium have pressure changes. Each heartbeat represent one filling and emptying of a heart, also called a cardiac cycle. Each beat creates a pulsation in the artery system and is caused by the pressure created by the contraction of the left ventricle. The blood is collected in the heart in the diastole and ejected in the systole. This is shown in Figure 2.6. The ventricle ejects the blood through isometric[8] and dynamic[9] contraction.

[8] An isometric muscle contraction is one in which the muscle fires but there is no movement at a joint. In other words, there is no change in the length of the muscle.

[9] Dynamic contraction refers to contraction where movement is involved

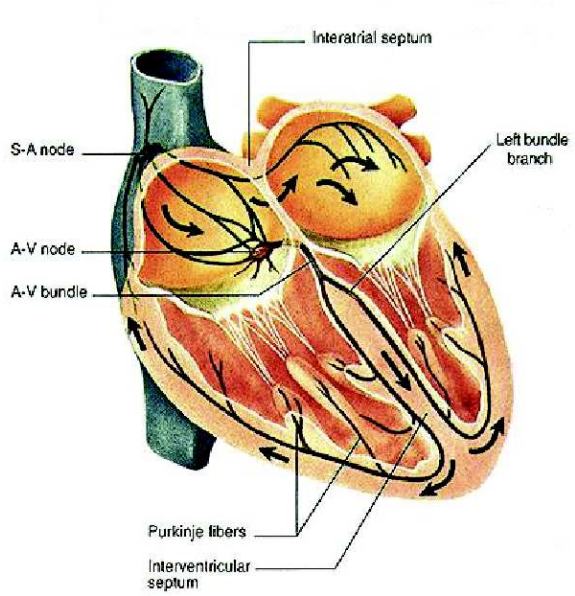

Figure 2.4: *The electric impulses in the heart. The figure shows how the electrical impulses are lead from the SA node to the AV node through the bundle of His, which is also called the AV-bundle of His, into the ventricle walls [Wikipedia, 2013b].*

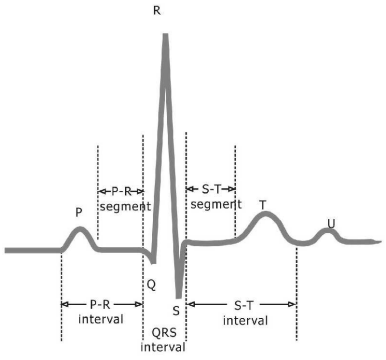

Figure 2.5: *Illustration of the ECG signature of the heart. The PQRS complex is displayed together with the different intervals [NationalInstruments, 2013].*

2.2.4 Electro cardiogram ECG

It is possible to measure the electrical signals generated in the heart. Small electrical sensors are placed on the outer surface of the body. This is called an electro cardiogram (ECG), and an example of a result is displayed in Figure 2.5. The heart generates an electrical signal which flows out from the

heart through the body. These impulses are almost equal each time. The body must be under no stress to get an accurate measure. The electrical activity is then converted into a graph. The contraction of the atria is associated with the ECG wave called the "P" as seen in Figure 2.5. The ventricular mass is large, so there is a large deflection of the ECG when the ventricles are depolarized, called the "QRS" complex. The re-polarization of the atria is hidden in the QRS complex. The "T" wave is associated with the return of the ventricular mass to its resting electrical start (re-polarization) [Hampton, 1973]. The letters P,Q,R,S and T are arbitrary chosen, and are all called waves.

2.2.5 ECG intervals

One type of analysis of the ECG graph is the distance duration of the waves and intervals between certain points in Figure 2.5. These point are relevant in order to establish a temporal relationship between the events during a cardiac cycle. The distances are expressed on a time axis, and are called the ECG intervals. The Q, R and S waves combined make a complex/interval, and the time between the S in the complex and the T wave is called the ST "segment". As seen in Figure 2.5 the different parts are labeled. The PR interval is measured form the beginning of the P wave to the beginning of the QRS complex. This is the time it takes for the excitation to spread from the SA node, through the aterial muscle and AV node, to the bundle of His onto the ventricular muscle. This interval is normally 120-200 ms long. The QRS interval normally has a duration of 120 ms or less. It is a measure of the time of spreading of impulses through the ventricle. Contraction is processed during the ST segment. The QT interval varies within the heart rate [Hampton, 1973].

2.2.6 Heart diseases

Heart diseases are divided into four categories, depending on which parts of the heart that is affected; the conduction system, coronary heart disease, the heart muscle or the valves.

Conduction system

The conduction system is the progression of impulses through the heart, which causes the heart to beat. Conduction diseases are normally caused by blockades of the bundle branches, that force the impulses to travel in an other route, which takes longer time. This causes one ventricle to contract one fraction of a second slower or later than the other, which is abnormal. And this makes it possible to have disorders in the conduction system. It is possible to have conduction disorders without having arrhythmia, but some arrhythmia's arise from conduction disorders.

Coronary heart disease

Coronary heart disease is caused by a narrowing or blockage of the coronary arteries. This can be caused by atherosclerosis(clogging/hardening of the arteries). Atherosclerosis is when cholesterol or fatty deposits builds up on the inner walls of the arteries. This may lead to restriction in the blood flow to the heart by clogging the artery, or by abnormal artery tone function. Without a sufficient blood supply, the heart will have lack of oxygen (ischemia) and the vital nutrients it needs to work propertly. Myocardial infaction, also known as a heart attack, is a possible result of a coronary heart disease. If a heart attack is left untreated for a substantial period of time, it can cause damage or death of the muscle tissue. Angina pectoralis is chest pain that is caused by ischemia due to obstruction or spasms in the coronary arteries.

Heart muscle

Cardiomyopathy is a measurable deterioration of the function of the heart muscle (myocardium). This may typically lead to heart failure, due to the reduction in the pump capacity of the heart. Heart failure occurs when the hearts pumping ability is reduced. Cardiomyopathy leads to a reduction in the heart's cardiac output[10]. A result of this will be that the heart is not able to meet the needs of the body and lungs. The body will then be congested with fluid because the hearts output can not properly match the venous return.

The valves

The common problems with heart valves are; regurgitation, steniosis and atresia. Regurgitation is backflow. That means if the valve does not close tightly, and the blood leaks back into the chambers rater than flowing forward through the heart or into an artery. Steniosis occurs if the flaps of a valve thicken, stiffen or fuse together. This makes it difficult for the heart valve to fully open, and not enough blood can flow through the valve. Some valves can have both steneosis and backflow problems. Atresia occurs if a heart valve lacks an opening for blood to pass through. Congenital heart valve disease often involves pulmonary or aortic valves that do not form properly. This can be so that the valves do not have enough tissue flaps, wrong shape or size, or missing an opening for proper blood flow. Acquired valve diseases usually involves aortic or mitral valves, and problems usually develop over time.

All heart diseases will more or less lead to a change in the hearts movement. Some of them can be detected using ECG.

[10]Volume of blood being pumped by the heart in one minute.

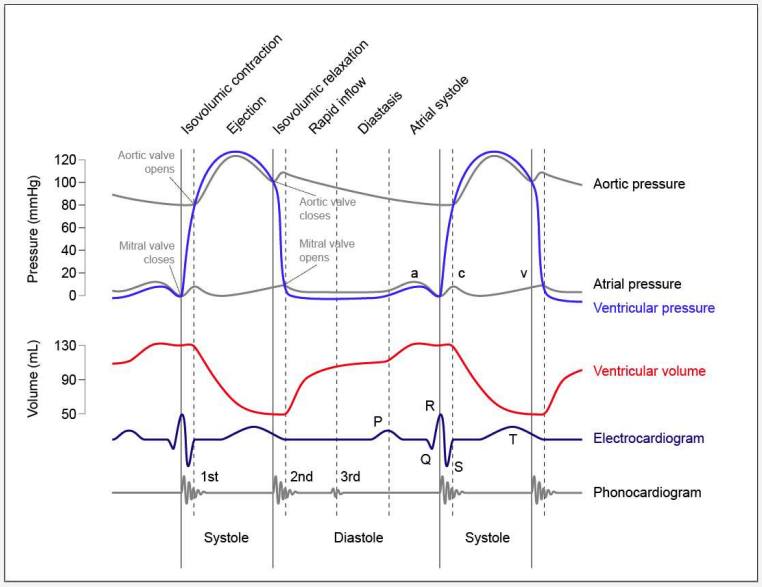

Figure 2.6: *Pressure changes in the heart during systole and diastole [Wikipedia, 2013c]. This figure shows the connection between ECG, heart sound and the pressure in right and left sides of the heart through the different phases of a cardiac cycle.*

2.2.7 Blood pressure

When the heart beats, it pumps blood through a system of blood vessels. The blood vessels transport blood through every part of the body. The force which the blood exerts on the walls of the blood vessels is called blood pressure. A cardiac cycle includes all the events that occur and is related to the variation in flow or blood pressure from the beginning to the end. Diastolic heart pressure is the minimum pressure in the arteries, which occurs near the beginning of the cardiac cycle, when the ventricles are filled with blood. Systolic blood pressure is the peak pressure in the arteries, which occurs near the end of the cardiac cycle, when the ventricles are contracting. In Figure 2.6 different curves are presented. The ECG and heart sound can be measured, but the blood pressure and the volume have to be estimated. (Or measured by a sensor placed inside the heart.) The curves presented in Figure 2.6 shows that when the aortic blood pressure is zero, the ECG is at its top (R). In the figure it is also possible to see how the different curves interact. The ECG and phonocardiogram curves are the only two non-invasive curves in the diagram. The other curves are estimates.

2.3 Similarity measures

The definitions of similarity measures used in this thesis are the similarity of two signal sequences or images X and Y, with the requirement that the sequences have equal length and the images are of equal size. An image similarity measure quantifies the degree of similarity between the intensity pattern in two images. This can both be two subsequent images/frames, or images/frames with a given interval. The choice of image similarity measure depends on the modality. In this project the similarity measures will be used on sequences with different length, to find where the two sequences are most equal. All the formulas will be given in the discrete domain. Similarity measures are used because we are working with subsequent frames where the idea is to see if there is a repetitive pattern in the cycles of frames.

2.3.1 Sum Absolute Difference

Sum of absolute difference (SAD) is one of the simplest similarity measures. It is found by calculating the minimum sum of absolute differences between two functions or sequences $\mathbf{X} = [x_1\ x_2 \cdots x_N]^T$ and $\mathbf{Y} = [y_1\ y_2 \cdots y_N]^T$, implied that they are different. The SAD is then defined as

$$SAD = \sum_{i=1}^{N} |x_i - y_i|, \tag{2.8}$$

where N is the length of the function/sequence. The smaller the value of SAD is, the more equal the sequences are. So we want to find the **Y**-sequence that is closest to matching **X**-sequence. It is typically used if we have several **X**-sequences, but only one **Y**-sequence, and want to find the **X**-sequence that is most similar to **Y**-sequence.

2.3.2 Correlation

Correlation is a measure of how two or more random/stochastic variables or sequence tend to vary from each other, the linear dependency. The most common or known method is the Pearson product-moment correlation coefficient (Pearson's correlation). Having two random sequences X and Y with expected values $\mu_x = \bar{X}$, $X = [x_1, x_2, \cdots, x_n,]$ and $\mu_y = \bar{Y}$, $Y = [y_1, y_2, \cdots, y_n]$ and the standard deviation $\sigma_x = \sqrt{\frac{1}{n}\sum_{i=1}^{n}(x_i - \mu_x)^2}$ and $\sigma_y = \sqrt{\frac{1}{n}\sum_{i=1}^{n}(y_i - \mu_y)^2}$ the correlation coefficient is defind as [Edwards, 1976]

$$\rho_{XY} = \frac{E[(X - \mu_X)(Y - \mu_Y)}{\sigma_X \sigma_Y}, \tag{2.9}$$

and estimated by

$$r_{xy} = \frac{\sum_{i=1}^{n}(x_i - \mu_x)(y_i - \mu_y)}{\sqrt{\sum_{i=1}^{n}(x_i - \mu_x)^2 \sum_{i=1}^{n}(y_i - \mu_y)^2}}, \tag{2.10}$$

where E is the expectation value and i represent a number of an element in a sequence of length n. If the Pearson correlation coefficient is $+1$ there is a perfect correlation/linear relationship between X and Y. If the correlation is 0 there is no relationship between X and Y, they are independent. If the coefficient is -1 there is a negative linear relationship between the variables X and Y.

2.4 Entropy

Entropy is the measure of uncertainty in a random sequence; said in an other way, it is the measure of the average amount of information required to describe the random sequence [Cover and Thomas, 1991]. The first order entropy H of a sequence $X = [x_1, x_2, \cdots, x_n,]$ is defined as

$$H(X) = -\sum_{i=1}^{n} p(x_i) \log_b(p(x_i)), \tag{2.11}$$

where $p(x_i)$ is the probability of an incident of the probability mass function, n is the length of the sequence with i elements and $H(X)$ is the entropy. The base of the logarithm depends on what is measured. log_2 is for example used for binary numbers, giving the information content in bits.

2.5 Mutual Information

Mutual information (MI) between two random variables is a measure of how much information one random variable contains of the other random variable. It is a measure of the reduction of uncertainty between two random variables when one of them is known [Cover and Thomas, 1991]. One of the advantages in MI is that there is no need for prior information about the random variables. It assumes that the statistical information can be captured with the joint entropy between the two random variables. The joint entropy between the two random variable distributions X and Y is defined as

$$H(X, Y) = -\sum_{x,y} p_{XY}(x, y) \log p_{XY}(x, y), \tag{2.12}$$

where P_{XY} is the joint probability distribution of the random variables X and Y.

Mutual information is defind as

$$I(X; Y) = H(X) + H(Y) - H(X, Y), \tag{2.13}$$

where $H(X)$ and $H(Y)$ is the entropy of the random variables. Mutual information is a robust measure to find outliers, it is efficient to calculate and has been used with success in the medical imaging domain.

2.6 Earth Movers Distance

Earth Mover's Distance (EMD) reflects the minimal cost that must be used to transform one signature or histogram into another. This can be associated with the well known transportation problem. Given two histograms P and Q where $p \in P$ and $q \in Q$ are bins in the histogram. Let's say that P's bins are piles of earth p and Q's bins are holes q in the ground. Then the earth mover's distance is the minimum cost of moving the piles of earth into the holes. The piles can be split and the cost of transporting the earth to the hole is the distance between the pile and the hole [Vahrenhold, 2009]. Then the EMD can be formalized by linear programing[11]. We then want to find the flow $F = f_{pq}$, where f_{pq} is the flow of earth from p to q and $D = d(p, q)$ is the distance between p and q that minimizes the overall cost,

$$WORK(P, Q, F) = \sum_{p \in P} \sum_{q \in Q} d(p, q) f_{pq}, \tag{2.14}$$

with constraints

$$\forall p \in P, \forall q \in \quad Q f_{pq} \geq 0, \tag{2.15}$$

$$\forall p \in P \quad \sum_{q \in Q} f_{pq} \leq w(p), \tag{2.16}$$

$$\forall q \in Q \quad \sum_{p \in P} f_{pq} \leq w(q), \tag{2.17}$$

$$\sum_{p \in P} \sum_{q \in Q} f_{pq} = min(\sum_{p \in P} w(p), \sum_{q \in Q} w(q)), \tag{2.18}$$

where w represent the weight of the piles of earth p and holes q. The first constraint allows moving earth from p to q and not visa versa. The next two constraints give limits to the amount of earth p that can be sent to one hole q by the weight; and the hole q to receive no more than the weight. The last constraint forces to move the maximum amount of earth as possible. When this is solved we have found the optimal flow F and we can define the earth mover's distance as the work normalized by the total flow

$$EMD(P, Q) = \frac{\sum_{p \in P} \sum_{q \in Q} d(p, q) f_{pq}}{\sum_{p \in P} \sum_{q \in Q} f_{pq}}. \tag{2.19}$$

[11] Linear programing is the solution in allocating limited resources to achieve the maximum profit or minimum cost, but it is only applicable where all the relations are linear, and can accommodate only a limited class of cost functions [Candes and Tao, 2005].

2.7 Optical flow description

Optical flow, or optic flow, is the pattern of apparent motion of objects, edges and surfaces in visual scenes caused by the relative motion between an observer (eye or camera) and the scene [Patel and Upadhyay, 2013b]. It can be defined as the flow of gray values in the image plane in time-varying images. The optical flow can be denoted as $\vec{v} = (v_x, v_y)$, where v_x and v_y are the x and y components of the optical flow vector at a point, respectively. There are many different ways to calculate optical flow, we have for example gradient based approaches, correlation based approaches, spatio-temporal energy based approaches and phase-based approaches. Optical flow is speckle tracking, but I will not use or go into detail about speckle tracking in this thesis. A mathematical description of optical flow is given below [Patel and Upadhyay, 2013a] and illustrated in Figure 2.7.

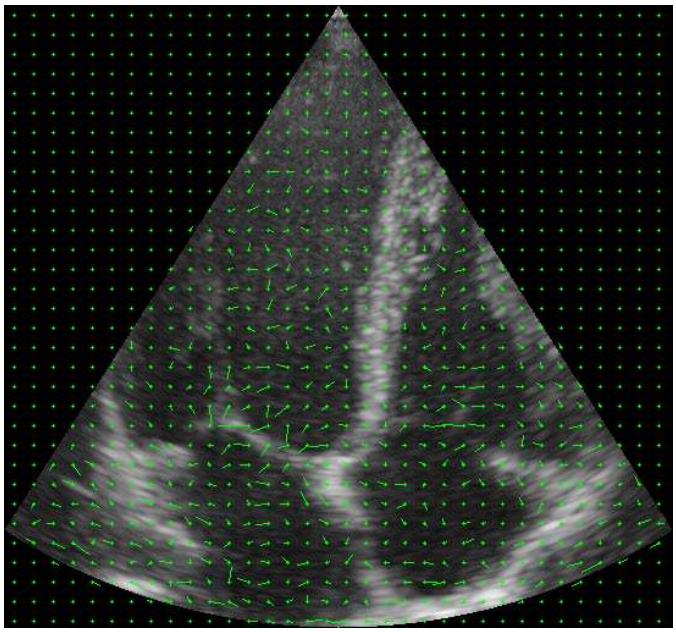

Figure 2.7: *The figure displays the optic flow between to subsequent images using the Färneback optic flow algorithm. The optic flow is calculated for each pixel in the image, but the optic flow arrows are estimated for every 16th pixel, so that it is possible to see the arrows and in which direction they are pointing.*

2.7.1 Mathematical explanation of optical flow

We let $I(x, y, t)$ denote the gray level value of an image (pattern) at pixel position (x, y) at time t. If we assume that the pattern is shifted by $(\delta x, \delta y)$

during a time increment δt (with no changes in intensity), we get the equation,

$$I(x, y, t) = I(x + \delta x, y + \delta y, t + \delta t). \tag{2.20}$$

Then $\delta x, \delta y$ will be the inter-frame displacement over the time interval δt. A Taylor series expansion of the right hand side of Eq.(2.20) gives

$$I(x+\delta x, y+\delta y, t+\delta t) = I(x, y, t) + \frac{\partial I}{\partial x}\delta x + \frac{\partial I}{\partial y}\delta y + \frac{\partial I}{\partial t}\delta t + H.O.T. \tag{2.21}$$

Higher Order Terms ($H.O.T$) will be ignored, assuming the local displacements δx and δy are small. By combining Eq. (2.20) and Eq. (2.21) and dividing by the non-zero time increment δt we get

$$\frac{\partial I}{\partial x}v_x + \frac{\partial I}{\partial y}v_y + \frac{\partial I}{\partial t} = 0, \tag{2.22}$$

where $v_x = \frac{\delta x}{\delta t}$ and $v_y = \frac{\delta y}{\delta t}$ are the x and y components of the estimated image velocity or optical flow, and $\nabla I = (\frac{\partial I}{\partial x}, \frac{\partial I}{\partial y})$ is the (spatial) intensity gradient at time t. The partial derivatives are normally written as

$$I_x = \frac{\partial I}{\partial x},\ I_y = \frac{\partial I}{\partial y},\ I_t = \frac{\partial I}{\partial t}. \tag{2.23}$$

Thus the equation can be rewritten more compactly as [Patel and Upadhyay, 2013b]

$$I_x v_x + I_y v_y = -I_t \quad \text{or} \tag{2.24}$$

$$\nabla I \cdot \vec{v} = -I_t. \tag{2.25}$$

2.7.2 Algorithm choice

As mentioned above there are many different approaches in implementing optical flow. Two different approaches are presented in this work. Lucas & Kanades (LK) dense optical flow algorithm [Lucas, 1985] and Gunnar Färnebaks dense optical flow algorithm [Farnebäck, 2002]. A dense optical flow means that all the pixels in the image are used. The other method is called sparse, where features in the image are found and tracked for example an edge or a corner. A sparse approach is often used in speckle tracking.

2.7.3 Lukas & Kanades algorithm

Lucas & Kanades algorithm is a popular method for optical flow estimation and computer vision [Lucas, 1985]. The method solves the basic optical flow equations for all the pixels in a neighborhood by the least squares criterion. It is a local method because it can not provide flow information in the interior

of uniform regions of the image. It assumes that the flow is more or less constant in a local neighborhood of the pixel that is being processed. Thus the optical flow equation can be assumed to hold for all pixels within a window centered at p. The local image flow (velocity) vector $\vec{v}(v_x, v_y)$ must satisfy Eq.(2.25),

$$\begin{aligned} I_x(q_1)v_x + I_y(q_1)v_y &= -I_t(q_1) \\ I_x(q_2)v_x + I_y(q_2)v_y &= -I_t(q_2) \\ &\vdots \\ I_x(q_n)v_x + I_y(q_n)v_y &= -I_t(q_n), \end{aligned}$$

where $q_1, q_2, \ldots, q_n$ are the pixels inside the window and $I_x(q_i), I_y(q_i), I_t(q_i)$ are the partial derivatives of the image I with respect to position x, y and time t, evaluated at the point q_i and at the current time. We can write these equation in matrix form

$$A = \begin{bmatrix} I_x(q_1) & I_y(q_1) \\ I_x(q_2) & I_y(q_2) \\ \vdots & \vdots \\ I_x(q_n) & I_y(q_n) \end{bmatrix}, \qquad v = \begin{bmatrix} V_x \\ V_y \end{bmatrix}, \quad \text{and} \quad b = \begin{bmatrix} -I_t(q_1) \\ -I_t(q_2) \\ \vdots \\ -I_t(q_n) \end{bmatrix}. \tag{2.26}$$

This system has more equations than unknowns and therefore it is usually over-determined. The Lucas & Kanade method finds a compromise solution by the least squares principle. It solves the 2×2 system,

$$A^T A v = A^T b \tag{2.27}$$

or

$$\mathrm{v} = (A^T A)^{-1} A^T b \tag{2.28}$$

where A^T is the transpose of matrix A. That is, it computes

$$\begin{bmatrix} V_x \\ V_y \end{bmatrix} = \begin{bmatrix} \sum_i I_x(q_i)^2 & \sum_i I_x(q_i) I_y(q_i) \\ \sum_i I_y(q_i) I_x(q_i) & \sum_i I_y(q_i)^2 \end{bmatrix}^{-1} \begin{bmatrix} -\sum_i I_x(q_i) I_t(q_i) \\ -\sum_i I_y(q_i) I_t(q_i) \end{bmatrix} \tag{2.29}$$

with the sums running from $i = 1$ to n. The window size normally used for Lucas & Kanade is 2 and 7 pixels in both the x and y direction. The choice of window size is decided by the movements in the image. If there is large movement in the image a large window size will be able to capture those movements. A small window prevents occlusions and "smooths out"

details in the image. It is also possible to weight the window so pixels close to the center have a higher weightfactor than the one close to the edge of the window [Fernando et al., 2007]. Use of pyramids will make it possible to detect large pixel movements without making the window size larger.

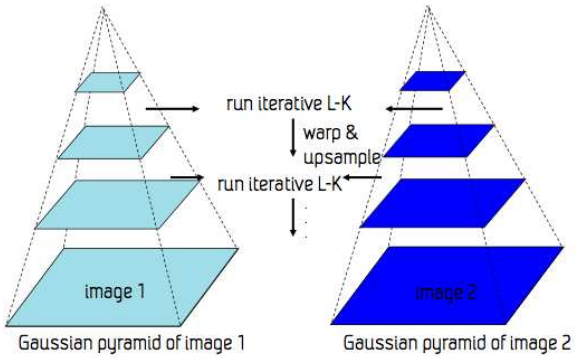

Figure 2.8: *The figure displays how two consecutive images are represented by pyramids and how the Lucas & Kanade algorithm is used [Berge, 2013].*

Lucas & Kanade with pyramid

When the pyramidal implementation is used, two images, I and J, are downsized to half the resolution at each new level in the pyramid. This is illustrated in Figure 2.8. The downsampling is done recursively with the original images in the bottom [Lucas, 1985]. The pyramid does normally not consist of more than 3-4 layers, because the resolution at the top layer will be too low. Before applying the pyramid implementation a Gaussian smoothing filter is used to prevent aliasing. Then the Lucas & Kanade algorithm is applied at each level in the pyramid. The window size in the Lucas & Kanade algorithm is the same. Therefore it is possible to detect larger movements in the images on the higher levels in the pyramid. This information is then used on the next pyramid level by warping the previous result onto the new result at the next level. At each level in the pyramid it is possible to iterate the displacement between the two images, I and J, so the displacement will be more accurate.
The algorithm can be described by the following steps: [Berge, 2013]

1. Take flow $\mathbf{u_{i-1}}, \mathbf{v_{i-1}}$ from level $\mathbf{i-1}$.
2. Use bi-linear interpolation to create $\mathbf{u_i^*}, \mathbf{v_i^*}$ matrices of twice the resolution of level $\mathbf{i}$.
3. Multiply $\mathbf{u_i^*}, \mathbf{v_i^*}$ by 2.
4. Compute $\mathbf{f_t}$ from a block displaced by $\mathbf{u_i^*(x,y)}, \mathbf{v_i^*(x,y)}$.

5. Apply LK to get $\mathbf{u_1'}, \mathbf{v_1'}$ the correction in flow.
6. Add the corrections, $\mathbf{u_1'}, \mathbf{v_1'}$ i.e $\mathbf{u_i} = \mathbf{u_i^*} + \mathbf{u_i'}, \mathbf{v_i} = \mathbf{v_i^*} + \mathbf{v_i'}$.

2.7.4 Farnebäcks optical flow algorithm

In image analysis it is possible to not only work directly on the image intensity values, but to also use methods that allow some kind of transform (often linear) of the data, e.g. Fourier transform, the Wavelet transform and all kinds of filters. Gunnar Farnebäck optical flow algorithm introduces a transformation called the polynomial expansion [Farnebäck, 2002]. The basic idea of polynomial expansion is to approximate a neighborhood of each pixel within a polynomial. It is important to assure that the polynomial coefficient capture sufficient information about the signal. The degree of the polynomial does not matter, but in Gunnar Farnebäcks algorithm a quadratic polynomial is used. A detailed explanation on Gunnar Farnebäcks algorithm can be studied in his PhD dissertation on Polynomial Expansion for Orientation and Motion Estimation from page 121-131 [Farnebäck, 2002]. A brief explanation of how the algorithm works is given below.

Explanation of Farnebäcks algorithm

Consider the quadratic polynomial

$$f_1(\mathbf{x}) = \mathbf{x^T A_1 x} + \mathbf{b_1^T x} + c_1, \tag{2.30}$$

where $\mathbf{A_1}$ is a real symmetric matrix, $\mathbf{b_1}$ is a real vector and c_1 is a scalar. We then construct a new signal f_2 with a global displacement $\mathbf{d}$,

$$\begin{aligned} f_2 &= f_1(\mathbf{x} - \mathbf{d}) \\ &= (\mathbf{x} - \mathbf{d})^T \mathbf{A_1} (\mathbf{x} - \mathbf{d}) + \mathbf{b_1}^T (\mathbf{x} - \mathbf{d}) + c_1 \\ &= \mathbf{x}^T \mathbf{A_1 x} - 2\mathbf{d}^T \mathbf{A_1 x} + \mathbf{d}^T \mathbf{A_1 d} + \mathbf{b_1}^T \mathbf{x} - \mathbf{b_1}^T \mathbf{d} + c_1 \\ &= \mathbf{x}^T \mathbf{A_1 x} + (\mathbf{b_1} - \mathbf{2A_1 d})^T \mathbf{x} + \mathbf{d}^T \mathbf{A_1 d} - \mathbf{b_1}^T \mathbf{d} + c_1 \\ &= \mathbf{x}^T \mathbf{A_2 x} + \mathbf{b_2}^T \mathbf{x} + c_1 \end{aligned} \tag{2.31}$$

In Eq. (2.31) we can write $\mathbf{x}^T \mathbf{A_1 d} - \mathbf{d}^T \mathbf{A_1 x} = 2\mathbf{d}^T \mathbf{A_1 x}$ since it is Hermittian. Equating the coefficients in the quadratic polynomial yields

$$\mathbf{A_2} = \mathbf{A_1}, \tag{2.32}$$

$$\mathbf{b_2} = \mathbf{b1} - \mathbf{2A_1 d}, \tag{2.33}$$

$$c_2 = \mathbf{d}^T \mathbf{A_1 d} - \mathbf{b_1}^T \mathbf{d} + c_1. \tag{2.34}$$

Here the important observation is that by Eq.(2.33) we can solve for the translation $\mathbf{d}$, at least if A_1 is non-singular,

$$2\mathbf{A_1}\mathbf{d} = -(\mathbf{b_2} - \mathbf{b_1}), \tag{2.35}$$

$$\mathbf{d} = -\frac{1}{2}\mathbf{A_1^{-1}}(\mathbf{b_2} - \mathbf{b_1}) \tag{2.36}$$

The Farnebäck algorithm can be described by the following steps[12]:

1. For each pixel in the image; compute the polynomial expansions $\mathbf{A}_1$, $\mathbf{b}_1$, c_1 and $\mathbf{A}_2$, $\mathbf{b}_2$, c_2 for image 1 and 2, respectively, using the area given by the user defined window.
2. Compute $\mathbf{A}$ and $\Delta\mathbf{b}$ according to $\mathbf{A} = \frac{\mathbf{A}_2(x,y)-\mathbf{A}_1(x,y)}{2}$ and $\Delta\mathbf{b}(x,y) = -\frac{1}{2}(\mathbf{b}_1(x,y) - \mathbf{b}_2(x,y))$.
3. Compute displacement vectors $\mathbf{d}$ by solving 2×2 equation system according to $\mathbf{d}(x,y) = \mathbf{A}(x,y)^{-1}\Delta\mathbf{b}(x,y)$.
4. Compute certainty values according to
   - $c_1 = \frac{d_x(x,y)^2}{d_x(x,y)^2+d_y(x,y)^2}$.
   - $c_2(x,y) = \begin{cases} 1, & d_{min} \leq d_x(x,y) \leq d_{max}, \\ 0, & \text{otherwise.} \end{cases}$
   - $c_3(x,y) = \begin{cases} 0, & (x,y)\text{within}\frac{N-1}{2}\text{pixels from the edge,} \\ 1, & \text{otherwise.} \end{cases}$
   - $c(x,y) = c_1(x,y)c_2(x,y)c_3(x,y)$.
5. Apply normalized averaging to the x component of the displacement computed in step 3, using a Gaussian applicability and c as certainty. This gives the final disparity estimates.

In the same way as Lucas & Kanade, the Farnebäck algorithm uses pyramidal implementation, with iterations at each level of the pyramid and a window. The choice of the window size depends on the same problems as for Lucas & Kanade. We also have to choose the neighborhood size used to find the polynomial expansion around each pixel. A large size means that the image will be approximated with smoother surfaces, yielding a more robust and more blurred motion field. We also have to be aware of the standard deviation of the Gaussian that is used to smooth the derivatives that are used as a basis for the polynomial expansion.

Both Lucas & Kanade and Färnebak's algorithms will be used. The implementations will be presented in Chapter 7, and results and discussions in Chapter 8.

[12]The steps in the algorithm are more detailed explained in [Farnebäck, 2002].

Chapter 3

The image data sets

The method and result are divided into two parts, Part I describes the histogram-based approach, and Part II the optical flow based approach. They are both with the purpose of finding a supplementary option to the ECG. Both parts will be presented with their methods and results subsequently, and then discussed. An overall discussion that compare the methods and results from the two different approaches will be given in the end.

3.1 Image acquisition and scan converting

All the images were recorded at GE-Vingmed in Oslo science park. The ultrasound scanner used was a Vivid E9. Two different probes were used; a 4V and a M5s [Healthcare, 2013]. Data were acquired at two point of times. The first recording was an apical four-chamber scan at different heart rates preformed on one healthy subject (me:-)) These data sets were stored in a limited RAW Dicom format. For the second recording, two different scans were acquired, an apical four-chamber scan and an apical long-axial scan. All scans where recorded at rest and after the subject had been put under stress. Four cardiac cycles were recorded and the scanner was set to use a default frame rate, and the acquisitions were saved in a more complete RAW Dicom format. A medical acquisition protocol was made (see appendix A.2) in order to ensure equal recordings for each test person. The recordings were performed on four healthy subjects, one female and three males between the age of 23 and 33. The acquisition was a part of a larger study-protocol approved by REK (Regional Ethics Committee). For the first recording, the only images available in the data sets were those that had been presented on screen during acquisition. These images where filtered to improve the visual image quality. An independent time aligned ECG was not available for these images. In the following, these images will be referred to as Dicom format images. For the second recording, it was possible to load the RAW Dicom files into GE's clinical workstation software Echopack and export the images

to a .h5 file format. The images then then stored were the unfiltered images. The time aligned ECG traces were saved together with the images. The .h5 format made it easier to upload the image data and the ECG data when using Matlab R2012a [MathWorks, 2013]. In the following, these images will be referred to as the .h5 format images. When exporting the files to the .h5 format the images were saved in polar coordinates. The images were therefore scanconverted back to Cartesian coordinates by using a bi-linear interpolation. This was done in a small Matlab script.

3.1.1 Choice of image format

Since we started up using histogram-based methods we thought that the Dicom format would be a good choice. The Dicom format consists of already filtered images, this to improve the image quality which would give a better result when using histogram-based methods. It later turned out that the first recordings were not saved in the complete RAW Dicom format and thus did not contain all the recorded information such as the ECG trace. In a RAW Dicom file the ECG tag can be found and dumped using PYDICOM. (This was done) Since the first dataset used was stored in a Dicom format that did not have the necessary information to easily extract the parts of the data needed for testing the algorithms, new datasets were recorded. These dataset turned out to be recorded on a later version of Echopack where the ECG trace was plotted on the displayed sector of the ultrasound acquisition. The new RAW dicom files would be very timeconsuming to use because all the data had to be collected from private tags. The .h5 data was not processed beforehand and was therefore more blurry which in theory would be better for the dense optical flow method. The .h5 format includes the class-information of the data, like the ECG. It was thus easier to use than the RAW Dicom format. The different storage formats became a problem when we wanted to use the data for testing the different methods. A lot of pre-processing had to be done before the data could be worked with in both cases. We therefore chose to use the first datasets that were recorded in Part I and the .h5 files converted from RAW dicom in Part II. This was also in compliance with the method used in Part I and Part II.

Chapter 4

Part I - Method

Histogram-based approaches

The main objective of this project was to find a mechanical signature of the heart similar to the ECG curve. In an attempt to achieve this, the following steps were performed in this first part;

- Reconstruct the first part of Aases algorithm described in the article: *Echocardiography without electrocardiogram* [Aase et al., 2011]. This is a method which uses the mean pixel intensity value of each frame to detect the cardiac cycle length. The various steps and choices made in the algorithm were examined. This was to better understand Aases choice of implementation. No attempt was made to estimate the starting point as done in the article, as this was regarded to be outside the scope of this thesis.

- When reading Aases article, we realized that his algorithm to detect the cardiac cycle length had a limitation with the heart rate boundaries that was not in accordance with our needs. An extention of the algorithm is therefore proposed to avoid the limitations of the cardiac heart rate to be between 45 and 90 bpm.

- If possible, find a mechanical signature of the hearth similar to the ECG curve. This by being inspired of the mean pixel intensity curve used by Aase, which did not completely meet these demands. We wanted to see what kind of curve entropy, mutual information and earth movers distance would give.

- If possible, find good features in the new curves calculated throughout the recordings, in the same way as for the ECG curve, both for a low and high pulserate.

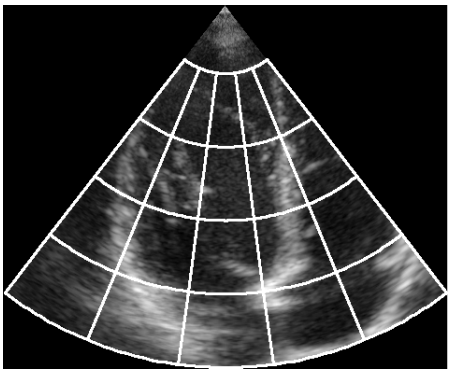

Figure 4.1: *One frame of a cycle is divided into 20 ROIs, each getting an index.*

4.1 Cardiac cycles length estimation

In the article *Electrocardiography without electrocardiogram* by Aase [Aase et al., 2011] a novel algorithm for detecting the cardiac cycle length was introduced. The idea was to calculate one or more 1D timeseries from a series of ultrasound frames. That is to represent each 2D-frame with one or a few features, in order to try to get a periodic time series with periodicity given by the heart rate. My implementation and interpretation of Aases SAD algorithm will first be presented in pseudo code, and then explained in more detail. For a given image sequence the algorithm was reconstructed as following:

Algorithm 1

1: Decide number of ROI
2: **for all** numbers i in ROI **do**
3: **for all** frames **do**
4: Calculate the mean pixel intensity value $\bar{P}(i)$
5: **end for**
6: Remove trend $P_{\text{trend}}(i)$ from $\bar{P}(i)$
7: Filter and differentiate ($P_{\text{F\&D}}(i)$) $P_{\text{trend}}(i)$
8: Calculate SAD(i) from $P_{\text{F\&D}}(i)$
9: **end for**
10: Decide cardiac cycle length or bpm from SAD(i)

Definition of ROI

In the first line of Algorithm 1 the total number of ROIs were defined. The acquisition frame was divided into ROIs because we want to look at

local changes in the image. The acquisition region is described using polar coordinates with the origin in apex. Each acquisition region was divided into azimuthal sectors with equal angular span and radial bins of equal length. The first 20% of the acqusition range related to the maximum range was discarded. Aase [Aase et al., 2011] used 20 ROIs; four in azimutal direction and five in radial direction as seen in Figure 4.1. We will see how different numbers of ROIs influence the result, if it would be an advantage to have more ROIs in radial direction or in azimuthal direction, or if this did not influence the result.

Calculation of mean pixel intensity

In Aases article, the calculation of the cardiac cycle length was based on B-mode pixel intensity values. Each ROI of a frame was reduced to one value, the mean pixel value of the ROI. The values were stored in a vector $\bar{\mathbf{P}}$, one for each ROI. This was done in line 4 of Algorithm 1.

Remove trend

In line 6 of Algorithm 1 the trend was removed. The trend is the slow variation in the curve. This was done to get the same starting point for each cardiac cycle. By fitting a second order polynomial to each mean pixel intensity curve and then subtracting it, the trend was removed. The second order polynomial was chosen on the basis of Aase's article [Aase et al., 2011].

Filter & Differentiate

In line 7 of Algorithm 1 the removed trend curve (P_{trend}) for each ROI was convolved with a Gaussian filter and a differentiating filter. A Gaussian filter is used to smooth out the small local variation of the curve. In the reconstruction of Aases algorithm this was done with a 5th order Gaussian smoothing filter. Other values were also tested out. The curve is differentiated to highlight where the intensity changes are big. The effect of not differentiating will also be tested out.

SAD algorithm

Line 8 of Algorithm 1 is the baseline in the SAD algorithm. The main idea behind the algorithm introduced by Aase [Aase et al., 2011] was to take an adequate part of the filtered and differentiated curve ($P_{\mathrm{F\&D}}(i)$) created for each ROI and use it as a template. When this was done, the template was matched against the rest of the curve using the similarity measure SAD, described in Chapter 2.3.1. The position of the minimum calculated SAD value will be the length of the cardiac cycle length. The length of the template will determine the minimum cycle length which is equivalent to the maximum heart rate. The method only wants one minimum point, so it was impossible to test the template on sequences more than two times the

template length. This determines the maximum cardiac cycle length, and the lowest heart rate possible. In Aases article the length of the recorded data (the time series of frame) was set to $T = 2$ seconds. The number of frames will depend on the sampling rate. Then in Aases algorithm,

- The first $\frac{T}{3}$ of the time series was used as a template T_t.
- The template was then from $\frac{T}{3} < t \leq \frac{2T}{3}$ stepped across the interval. For each t within the interval a new SAD was calculated. The minimum value of all the calculated SADs, is where the two functions are most equal. This is shown in the bottom plot of Figure 4.2.
- Repeat for all ROIs.

Aase commented on his restriction in the article [Aase et al., 2011]: *That the SAD curve only got one peak by setting the template* $> \frac{T}{3}$*. The algorithm for the detectable cardiac cycle* T_c *length would also have some limitations. The minimum cycle length* T_c *was limited by template length* T_t*. The maximum cycle length was limited as* $T_c < T - T_t < 2T/3$*. This would give a maximum cycle length at 01.33s and minimum bpm 45 and a minimum cycle length 0.67s with maximum hearth rate 90.*

The correct cycle length was verified with these criteria:

- Determine the median of the estimated cycle length from all ROIs. All the cardiac cycle length estimates that are less than 50 ms different from the median, are used as confidence measure, this according to Aases article [Aase et al., 2011]. If this condition holds, the cardiac cycle length is estimated. Otherwise the next step is needed.
- If less than 8 of the 20 ROIs (40%) are outside the confidence measure, the algorithm can be repeated up to two more times by restarting the algorithm 200 ms later.

If the last step did not hold, the SAD algorithm failed.

4.2 Correlation algorithm

As an alternative similarity measure to SAD, correlation could be used. The procedure would still be the same, except for step 8 in Algorithm 2.3.1, that had to be changed. As for the SAD algorithm, the first $\frac{T}{3}$ of the time series is defined as a template T_t. Then the template is matched in the same way as described in the SAD algorithm, calculating a new correlation coefficient each time the template was stepped across the the interval $\frac{T}{3} < t \leq \frac{2T}{3}$. The maximum value of the resulting curve was the estimated cardiac cycle length for a given ROI as seen in Figure 4.3.

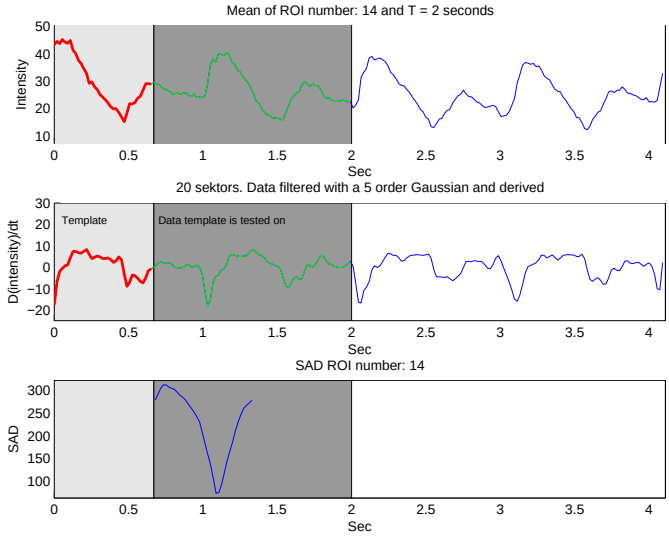

Figure 4.2: *Plot of the intensity curve, the differentiated intensity curve and the result from the SAD algorithm. The light gray area with the red curve is the area of the template. The dark gray area with the green curve is the area where the template and dataset were matched. The white area with the blue curve is the rest of the dataset, which was not used.*

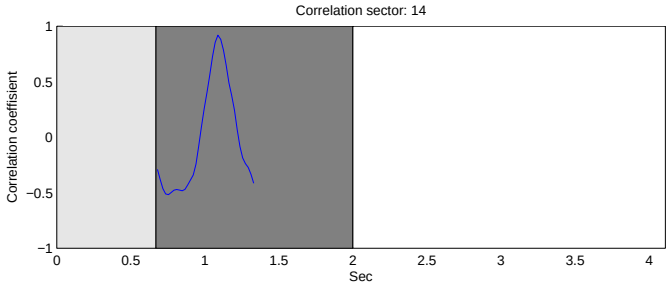

Figure 4.3: *Plot of correlation coefficient for detecting the cardiac cyclelength.*

4.3 Extension of cardiac cycle length algorithm

In the SAD algorithm introduced by Aase [Aase et al., 2011] there were some limitations. The upper and lower boundaries of the heart rate were controlled by the data length used. When setting $T = 2$ (length of the recorded data) as done in the article, the minimum and maximum heart rate were limited to 45 and 90 bpm, respectively. In his article Aase discussed his boundary selections when he described the algorithm design choices [Aase et al., 2011].

We wanted to see if it was possible to extend the algorithm to avoid the

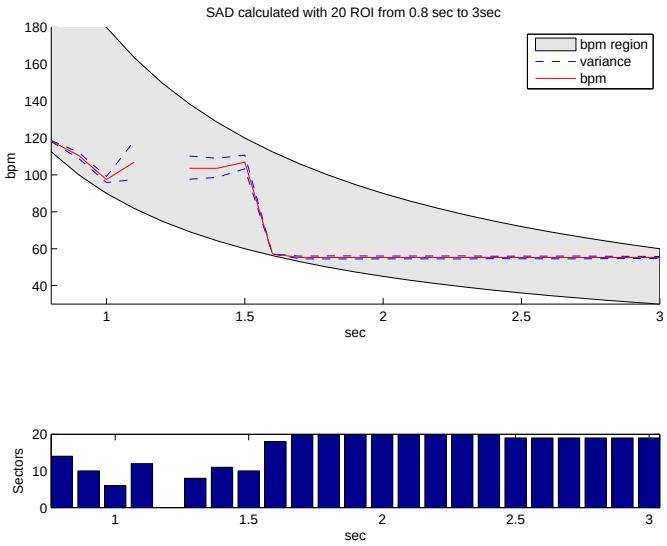

Figure 4.4: *The new expanded cardiac cyclelength detection algorithm using SAD. The detection starts from* $T = 0.8$ *seconds to* $T = 3$ *seconds, calculation SAD for each timestep. The upper panel of the figure displays the bpm found and also the upper and lower bpm boundary. The lower panel displays number of sectors within the confidence interval for each time step calculation.*

restrictions on the bpm boundaries, but still keep the constraint of only getting one peak in the SAD curve. A possible approach to achieve this was based on estimating the heart rate for several choices of the data length T, and then combine all of these results into one robust estimate. A procedure of how this can be done, is given below:

1. A bmp was estimated for each T between 0.8 seconds and 3.0 seconds in steps of 0.1 seconds (bmp(T)). The minimum heart rate would then be 30 bpm and the maximum heart rate 250 bpm. This was done either by the SAD or the correlation algorithm described in Chapter 4.1 and Chapter 4.2. The requirements of the T_t (template) from Aases article are retained by always letting $T_t < \frac{T}{3}$ for each step of T.

2. Then:

   - Verify that the number of ROIs were within the minimum 40 % requirement set by Aase, which is explained in Chapter 4.1. If the requirement was not fulfilled, the bpm value could not be further used.
   - Check that the bpm(T) value was within a $\pm 3\%$ interval of the previous estimated bmp value (bmp($T-1$)). The 3% confidence

interval was chosen on the basis that a higher bpm gives faster variation than a lower bpm.

- Make sure the bmp value of the estimated T was valid, the bmp was checked to be within the upper and lower bmp boundaries for the given T.

3. The number of steps T that can be found within upper and lower bpm boundaries was calculated for the given bmp value.
4. The number of approved estimated bmp values within these boundaries was counted.
5. If 70% of the estimated bpm values were within the upper and lower bpm bonderies, the mean of the bpm values was calculated and used as the final bpm value. The procedure was then stopped.

An illustration of the procedure is given in Figure 4.4 where the SAD algorithm is run from $T = 0.8$ seconds to $T = 3$ seconds in step of 0.8 seconds.

4.4 Histogram-based approaches

In the end of this first part we want two see if it is possible to use some other measures than the mean pixel intensity, to find a new method to detect a curve of the hearts movement pattern similar to ECG. Even though the curves of a low heart rate recording in the upper plot in Figure 4.2 showed some periodic patterns, it appeared that much of the repetitive pattern disappeared for a high heart rate recording. There were also only small similarities in the recordings between a high pulse and a low pulse recording done on the same person. This is shown in Figure 5.11 to Figure 5.13 in Chapter 5.4.1. This would make it difficult to use this method as an alternative to the ECG. Thus other histogram-based approaches was tested out.

4.4.1 Mean intensity pixel value

Since this thesis was inspired by Aases algorithm where the mean pixel intensity was calculated through a timeseries of ultrasound B-mode frames, we started by looking at how the mean pixel intensity pixel values changed throughout time by calculating a curve for different numbers of ROIs. For each ROI we first got a curve of pixel intensity per time/frame. This was used as a reference curve when testing the histogram-based approaches.

4.4.2 Entropy implementation

In Chapter 2.4 we saw that entropy was a measure of disorder. The image entropy was implemented as described in Chapter 2.4. For each frame of

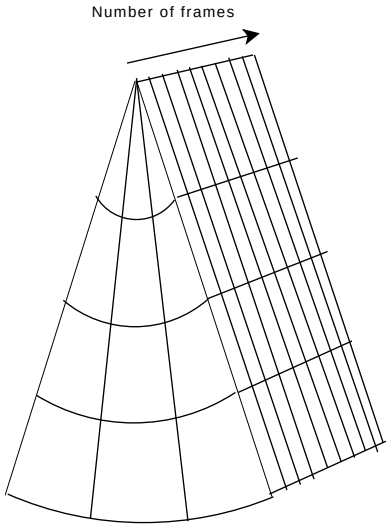

Figure 4.5: *Figure of the ROI throughout a time series of frames.*

the recording the entropy was calculated in the same way as for the mean intensity curve. The result of the entropy calculation gives the entropy as a function of frame/time. The entropy was calculated for 1, 9 and 20 ROIs. An illustration of 9 ROIs is given in Figure 4.5.

4.4.3 Mutual information implementation

The mutual information algorithm described in Chapter 2.5 is a measure of common information between two frames. Two consecutive frames were used and the similarity between those two frames were calculated. The frames were still B-mode intensity images. This was done for all ROIs throughout the time series of frames giving a function of mutual information per frame/time. Mutual information as a function of frame/time was calculated for 1, 9 (3 radial bins $\times$ 3 azimuthal sectors) and 20 (4 radial bins $\times$ azimuthal sectors) ROIs.

4.4.4 Earth Mover's distance implementation

The earth mover's distance described in Chapter 2.6 was implemented in the same way as mutual information, but here we looked at differences between two subsequent frames to see how much work that had to be performed to make the two histograms equal. This gave a EMD value between two ROI frames as a function of frames or time. The Earth mover's distance was calculated for 1, 9 and 20 ROIs as functions of frame/time.

Chapter 5

Part I - Results and Discussion

In the first part of Chapter 4 we started reconstructing Aases algorithm [Aase et al., 2011]. The result of reconstructing the algorithm, examining and extending it will be given below. Part I will also give the results of using other similarity analysis. The results will be discussed as they are presented.

5.1 Reconstruction of the SAD algorithm

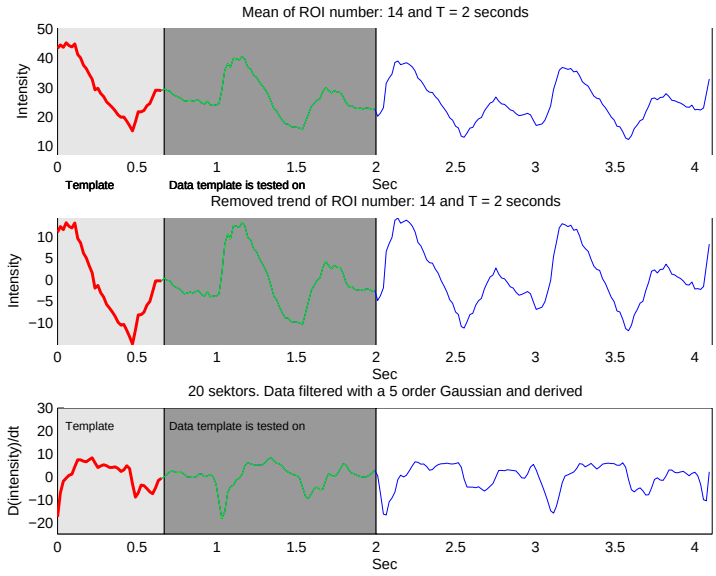

Figure 5.1: *The upper plot is of the mean pixel intensity values throughout a timeseries for frames. The second plot is of the mean pixel intensity curve when the trend is removed. The bottom plot is the differentiated intensity curve.*

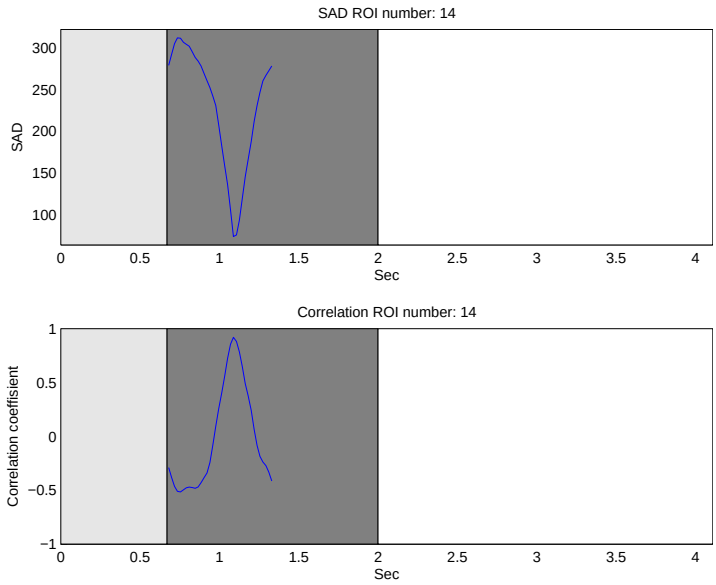

Figure 5.2: *The first plot is of the estimated SADs. The length of the estimated cardiac cycle is where the curve get its minimum value. The second plot is of the estimated correlation coefficients. Where the curve get its maximum value, is the length of a cardiac cycle.*

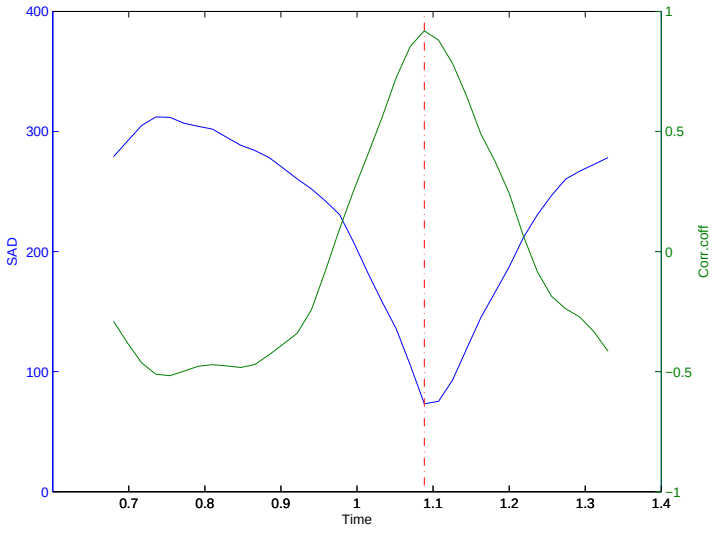

Figure 5.3: *The plot displays where the minimum SAD value and maximun correlation value occurs at the same point at the same time for both methods. The plot is of ROI number 14.*

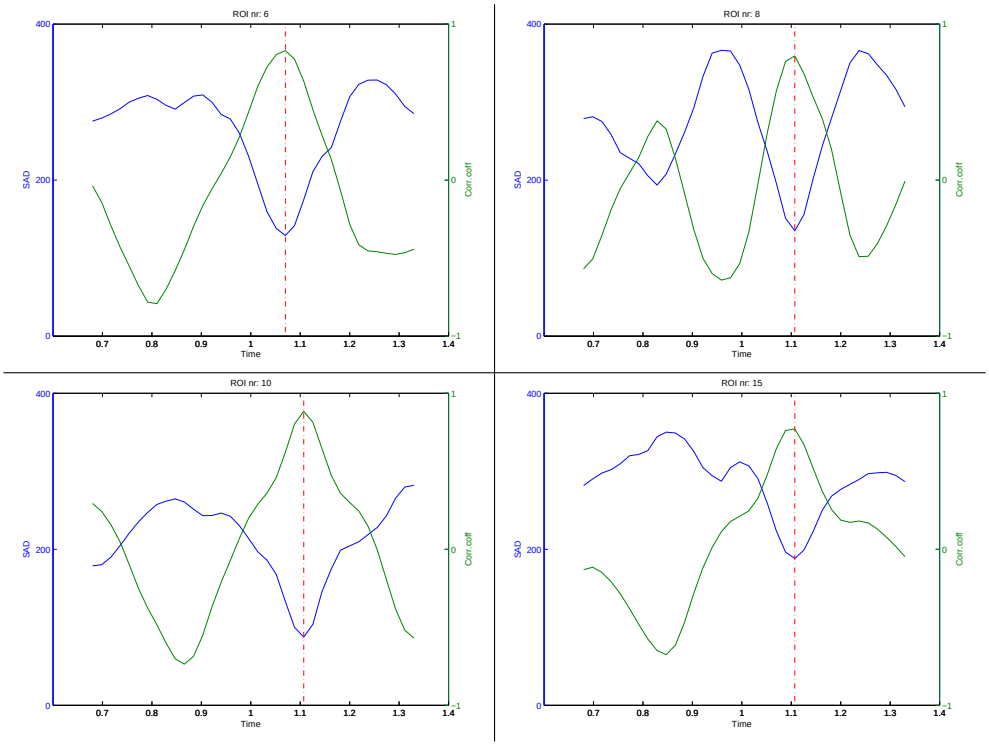

Figure 5.4: *The plots display where the minimum SAD value and maximun correlation value occurs at the same at the same time for both methods. The plot is of ROI number 6, 8, 10 and 15.*

From the result in Figure 5.1 we see at the top panel, the plot of the mean pixel intensity estimated over several cardiac cycles for ROI 14 out of 20 ROIs. The mid panel displays the plot of the intensity curve when the the slow movements spanning the mean curve throughout the cardiac cycle are removed. The third plot in Figure 5.1 is of the differentiated intensity curve after filtering and smoothing. The mean pixel intensity curve is differentiated in order to make it easier to detect the changes in curve. The upper plot in Figure 5.2 is of the SAD curve that was calculated. As seen in the plot, the SAD curve gets a dip. The position of the minimum value of the dip is the estimated length of the cardiac cycle. The upper and bottom plot in Figure 5.1 and upper plot in Figure 5.2 are the same plots as displayed in Aases article.

5.1.1 Similarity Measure: Correlation

In the bottom plot of Figure 5.2 correlation was used as a similarity measure. The correlation curve gets a peak where the correlation coefficient is at its highest. As seen in the two curves in Figure 5.3, the peak and the dip have their maximum and minimum value at the same time t. In this example ROI 14 is displayed. As seen in Figure 5.3 this occurs at t equal to 1.09 seconds, which gives the cycle length. The estimation was done in frames so the frame number had to be converted to time depending on the framerate. The time was again converted to bpm to get the heart rate. In this example the heart rate was estimated to 55 bpm from the equation $\frac{60\,seconds}{cyclelength}$. The results displayed in Figure 5.3 shows that both algorithms are able to detect the cardiac cycle length. This is confirmed from the plots in Figure 5.4 where we see that it is not only ROI number 14 that has corresponding minimum and maximum values. When testing the correlation as a similarity measurement, the same parameter restrictions from Aase [Aase et al., 2011] for constructing the SAD were used.

5.1.2 Testing different parameters

The analysis was based on two datasets from one subject. One with a high bpm, called high recording, and one with a low bpm called low recording. Since we only used two datasets it was difficult to draw firm conclusions on the robustness. We do however get a picture of how the algorithms work. The quality of the acquisitions was good. The diagrams in Figure 5.5 and Figure 5.6 display results for the SAD and correlation algorithms run with different parameters. The figures consists of two acquisitions, for a low and high recording, with respectively 1, 9, 20, 49 and 100 ROIs. The diagrams display how the different parameters for the SAD and correlation algorithm affect the result. The parameter adjustments made beside the number of ROIs, was the order of the Gaussian filter, and whether the curve was differentiated

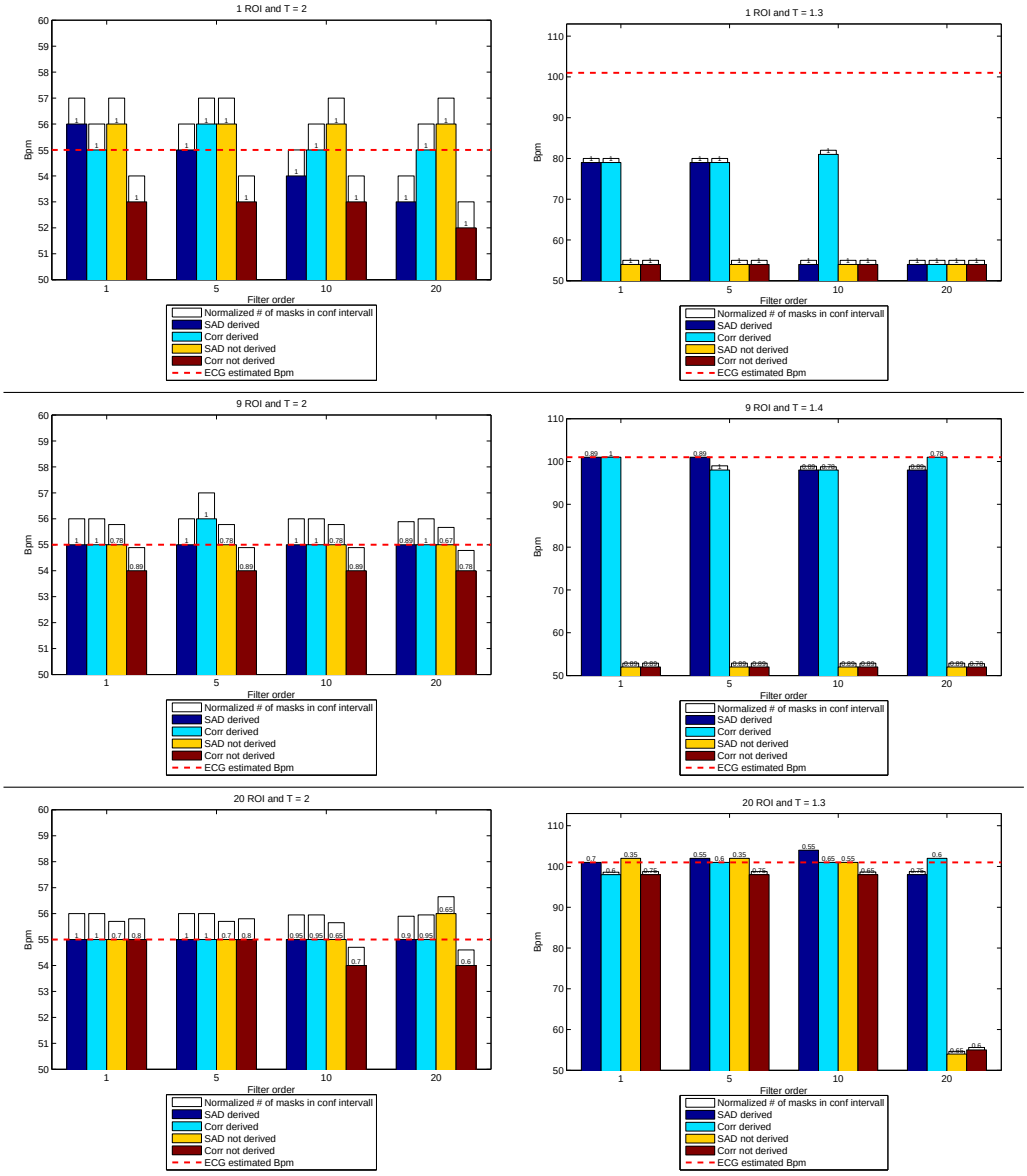

Figure 5.5: *The figures show the SAD and correlation algorithm for a low (left side) and high (right side) bpm compared against each other. The bars display how different parameters influence the cycle length estimation. The upper plots are of 1 ROI (Global), the middle plots are of 9 ROIs (3x3) and the bottom plots are of 20 ROIs (4x5).*

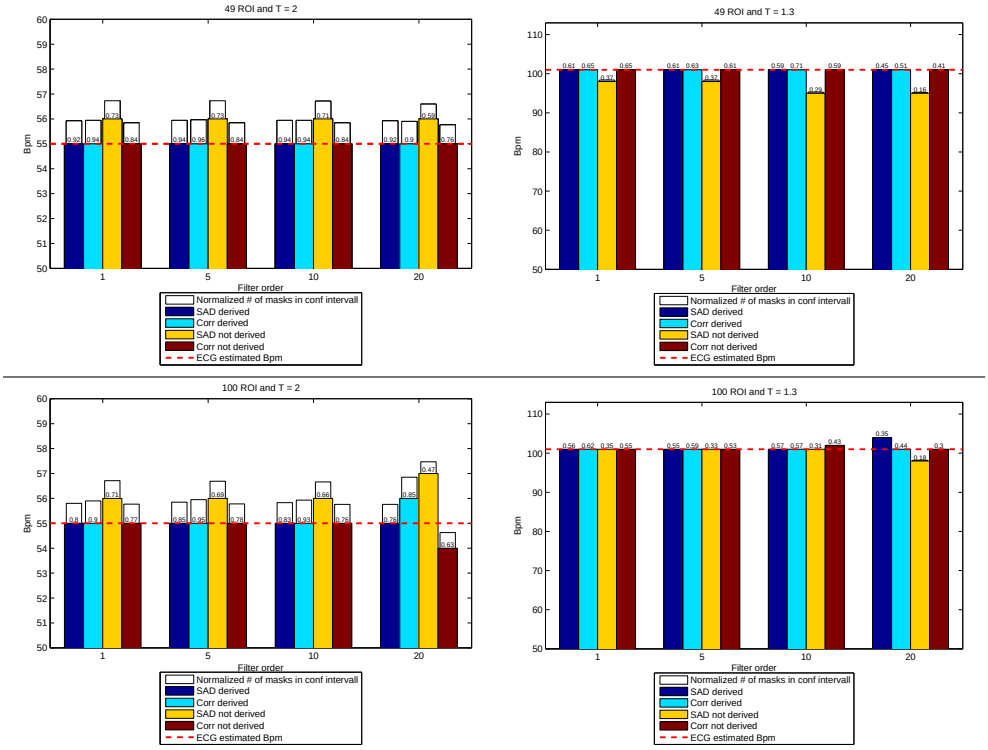

Figure 5.6: *The figures show the SAD and correlation algorithm for a low (left side) and high (right side) bpm compared against each other. The bars display how different parameters influence the cycle length estimation. The upper plots are of 49 ROIs (7x7) and the bottom plots are of 100 ROIs (10x10).*

or not. The bars in the diagrams are assigned one color each, to indicate whether the calculated SAD and correlation was differentiated or not. The little bar on the top gives the normalized number of ROI

$$\text{Normalized}_{ROI} = \frac{\text{Number of ROIs in confidence interval}}{\text{Total number of ROI}}. \tag{5.1}$$

The dashed red line is the known bpm value retrieved from the ECG recordings. The results from the varying the parameters shown in the diagrams are discussed in the points below. The explicit numbers for the calculations are given in the tables in Appendix A.1 for most of the iterations. The SAD and correlation algorithms were run at $T = 2s$ and $T = 1.3s$ for the low and high recording respectively.

- When the number of ROI was set to 1 the upper left diagram of Figure 5.5 shows that there are some variation in the estimated bpm for the low bpm recording. The correlation algorithm seems more dependent on differentiation than on the SAD algorithm. A low filter order seems more desirable than a high filter order. The normalized ROI will always be one when only one region is selected. For the high recording as seen in the upper right diagram in Figure 5.5, all the tested parameter sets make the algorithm fail when trying to estimate the bpm.

- When the ROI was increased to 9 ROIs, the middle left diagram in Figure 5.5 shows that the methods were more robust and quite accurate for all parameters at a low recording. This is also evident for the high recording seen in the middle right diagram of Figure 5.5 where both SAD and correlation manage to estimate the right bpm when the input curve was differentiated and for all different orders of the Gaussian smoothing filter. The normalized ROIs are high where the differentiation is used. This indicates the need for differentiation. The method fails for the non differentiated SAD and correlation for the high bpm recording for all filter values.

- For 20 ROIs the bpm values for both high and low recording are quite accurate. The bottom right diagram in Figure 5.5 shows that it is only the highest filter order that really fails, when the curves were not differentiated. The pulse is also not 100% accurate for all values, it varies with ± 2 bpm. But this would not be outside the limit of what is accepted. For the low bpm recording displayed in Figure 5.5 all estimated values would be inside what is acceptable.

- The 49 ROIs diagrams for low and high bpm seen in the upper left and right diagram of Figure 5.6 shows that the estimation had more or less the same accuracy when the number of ROIs was increased. The same has to be said for the high bpm recording. We can see that the

normalized value of ROIs has decreased, but this can be because the ROIs get smaller and therefore do not contain so much information.

- From the two bottom diagrams in Figure 5.6 with 100 ROIs it is seen that for the high recording the estimations were almost accurate for all different parameters when the order of the filter was set to 20. The low recording seen in Figure 5.6 shows that the calculation with a 20 order Gaussian smoothing filter fail to estimate the bpm for all other methods than the SAD, when the curve was differentiated. Also here we see that the normalized value of ROIs had decreased even more, but the ROIs have also gotten even smaller.

5.1.3 Discussion - Reconstruction of the SAD algorithm

The diagrams in Figure 5.5 and Figure 5.6 displays that for one ROI, using the global mean pixel intensity value, the SAD and correlation algorithms will fail. It also shows that it is possible to get the same results with fewer numbers of ROIs than the 20 ROIs Aase used, but the result will be more reliable when a larger number of ROIs are used. It also shows that if the order of the smoothing filter is to high, it will affect the result negative when the curve is differentiated and also that the differentiation makes the algorithm more robust. The drawback with having a large number of ROIs is that the calculation time will increase and the algorithm runs slower. Since we were not able to get so many recordings it has been difficult to really test the robustness of the influence of the parameters. The estimation done were on recordings with good acquisition. The comparison of SAD and correlation tells that there are not much difference in which of these two similarity measures that are used. None of them really stand out to give more accurate results than the other. What we can say out of all this is that the number of ROIs chosen in Aases article and the method used is a good and reasonable choice.

5.2 Extension of the algorithm

Figure 5.7 to Figure 5.10 are visual results of how the extended cardiac cycle length algorithm works. The plots show the bpm value for a calculated step t, between 0.8 and 3 seconds. The numbers of ROIs that are used to decide the bpm value are displayed as a bar in the bar plot below. Figure 5.7 and Figure 5.8 are of 20 ROIs when SAD and correlation are used as similarity measures. They are of a low and high bpm recording respectively. Figure 5.9 and Figure 5.10 illustrates the same, only with 9 ROIs. The light gray area in the figures is the minimum and maximum bpm area. The variance of the estimated bpm values in the confidence measures is also plotted to show the discrepancy of the estimations.

The results from the Figure 5.7 and Figure 5.8 show that when 20 ROIs were used for both a low and high bpm recording, both similarity measures manage to estimate the correct pulse[1]. From Figure 5.7 we see that we get a bpm estimations for low values of t, but these do not fulfill the conditions given in the extended algorithm in Chapter 4.3. It was only at higher values of t that these conditions were fulfilled. As illustrated in Figure 5.7, the heart rate would be 55, which was the same as shown in the reconstruction of Aases algorithm. In Figure 5.8 we see that the conditions to the extended algorithm were met for lower values of t, and according to the conditions the algorithm was stopped when the conditions were met. As we can read from the plot, the pulse would be 102 bpm which was the same as the calculated bpm from the ECG.

Figure 5.9 and Figure 5.10 are with 9 ROIs. As we can see the extended algorithms manage to give the same results as for 20 ROIs, although some of the estimations for some values of t are not the same between the two choices of ROIs and are outside the bpm limits as seen in Figure 5.9. From Figure 5.10 we see that the number of ROIs used as one of the conditions in the extended algorithm are the same as for 20 ROIs. This would make the extended algorithm more robust.

5.3 Discussion - Extended algorithm

The implementation done in this project was just a proposal of how the algorithm could be extended. There are variables that might could have been different to do a quality check or make the proposed algorithm run smoother. First and most importantly, the results from the extended algorithm displayed in this report is just of two data recordings of the same person, one high bpm recording and one low bpm recording. The dataset consisted of two good acquisitions. The extended algorithm was tested on more data sets, but they were all from good acquisitions and also from the same test person. Since the basis of the recorded dataset was not wide enough, it was impossible to make a quantitative statistical calculation and test the robustness of the extended algorithm.

The steps in the algorithm could maybe also have been longer. There was maybe no need to have steps for every 0.1 second in the time interval. Then the number of subsequent values also would have been changed. The conditions that estimated the bpm value could not differ more than 3% of the previous estimated bpm value, which was a fixed value, and this requirement could have been tested out and adjusted accordingly. Also the requirement that 70% of the bpm values had to be within the upper and lower bpm limits were fulfilled, but this also could have been adjusted with furthur testing to

[1]Both the high and low recording was done with ECG so the correct bpm could be used as a reference.

conclude that the correct bpm was found. This would have been easier to do if we had more datasets from different persons with various heart rates. The extended algorithm also required that the recorded data was 3 seconds long, so it could detect a low heart rate.

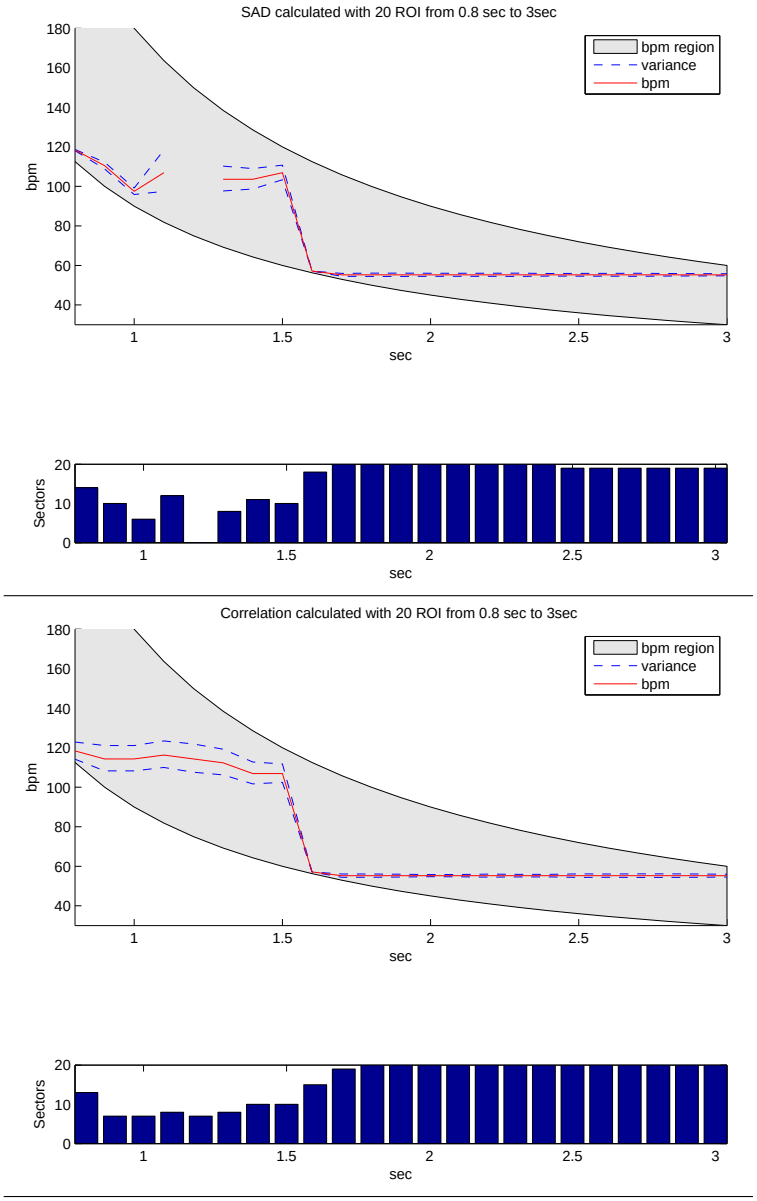

Figure 5.7: *The plots are of the extended cardiac cycle length algorithm. The upper plot using SAD as a similarity measure, and the bottom plot using correlation as a similarity measure. The plots are tested on a low bpm data set and uses 20 ROIs. The estimated heart rate from the ECG was 55 bpm.*

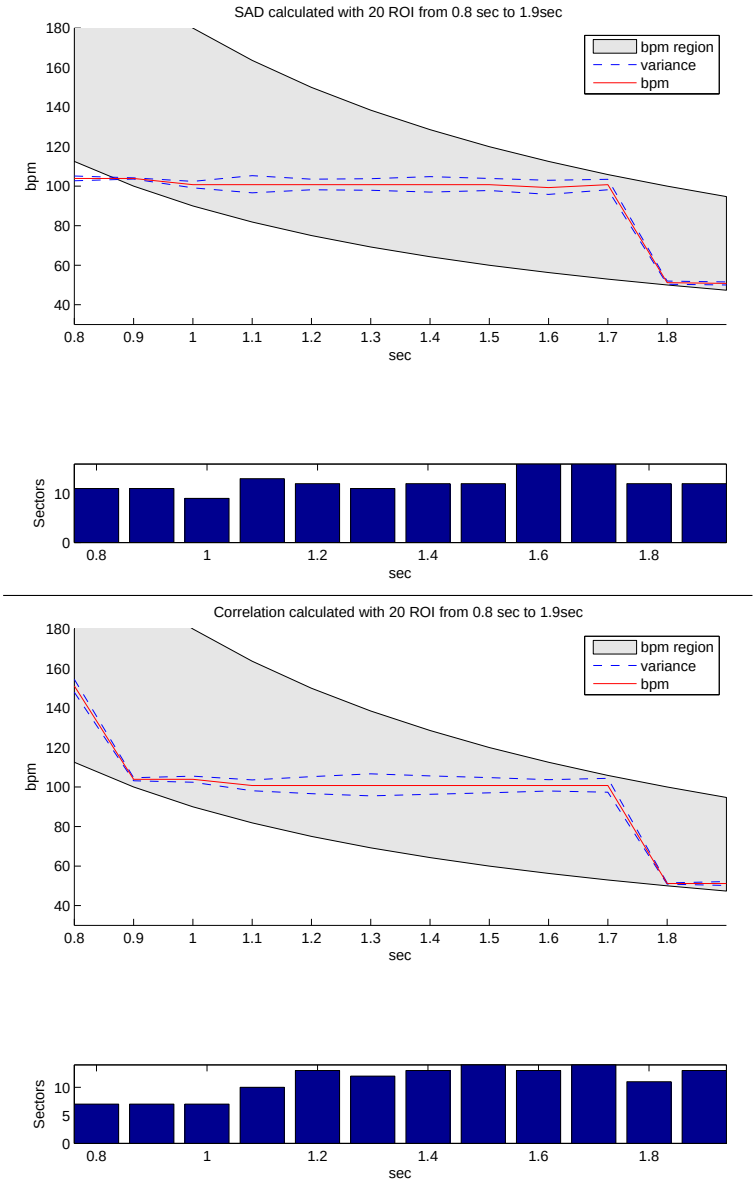

Figure 5.8: *The plots are of the extended cardiac cycle length algorithm. The upper plot using SAD as a similarity measure, and the bottom plot using correlation as a similarity measure. The plots are tested on a high bpm data set and uses 20 ROIs. The estimated heart rate from the ECG was 102 bpm.*

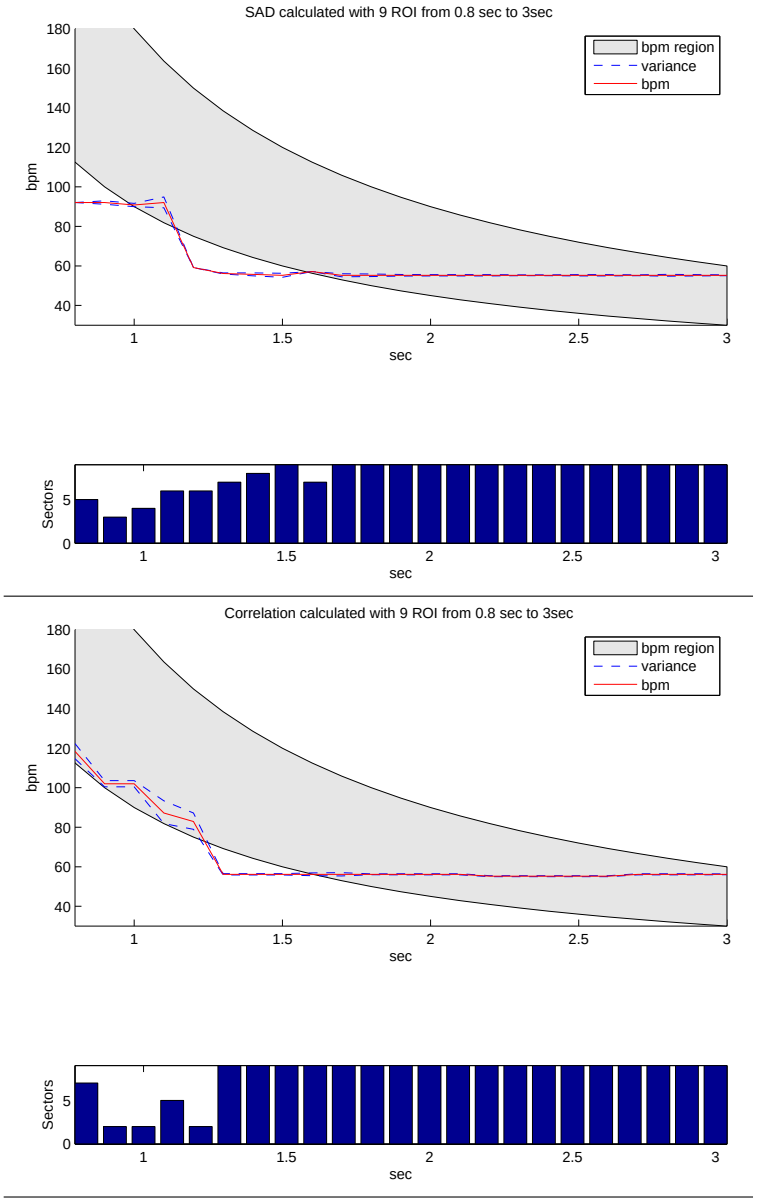

Figure 5.9: *The plots are of the extended cardiac cycle length algorithm. The upper plot using SAD as a similarity measure, and the bottom plot using correlation as a similarity measure. The plots are tested on a low bpm data set and uses 9 ROIs. The estimated heart rate from the ECG was 55 bpm.*

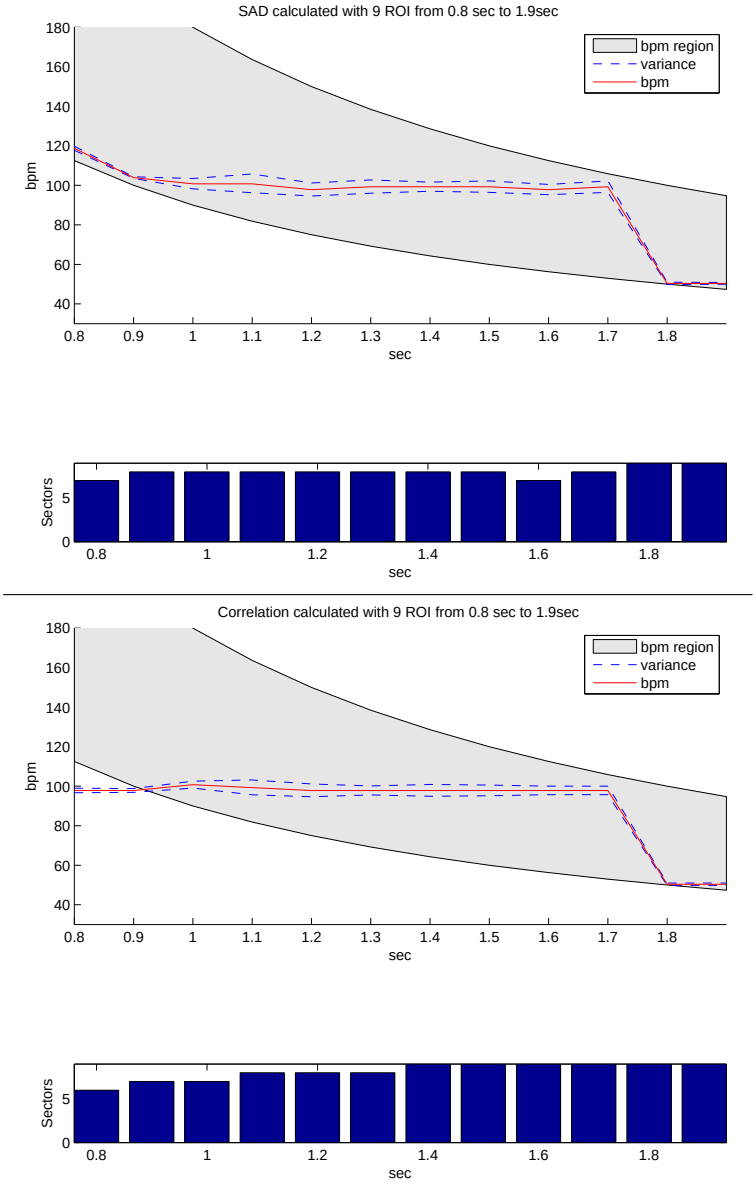

Figure 5.10: itThe plots are of the extended cardiac cycle length algorithm. The upper plot using SAD as a similarity measure, and the bottom plot using correlation as a similarity measure. The plots are tested on a high bpm data set and uses 9 ROIs. The estimated heart rate from the ECG was 102 bpm.

5.4 Results of using other similarity analyzes

One of the overall goals for this project was to see if it was possible to find a repetitive pattern at different bpms. Aases algorithm [Aase et al., 2011] used the mean pixel intensity value as the curve for calculating SAD. Below are the results of how other histogram-based approaches of finding a curve came out with different numbers of ROIs throughout four cardiac cycles.

5.4.1 Mean pixel intensities

The result from calculating the mean pixel intensity for the curve of 1, 9 and 20 ROI are given in Figure 5.11 to Figure 5.13. The results are demonstrated with a low and high recording to see if there are some coincident patterns in the curves. The curve for 1 ROI of a low bpm recording gives an intuition that it might be possible to find a repeating pattern as we can see in the left plot of Figure 5.11. Each cardiac cycle is marked with a vertical dashed red line and we see that between each of the red dashed lines the curve gets a minimum value that seems to occur at the same phase of the cycle. In the right plot in Figure 5.11 of the high recording of bpm, this pattern does not occur. The same pattern occurs for 9 ROIs as for 20 ROIs. In the low recording we get a repetitive pattern for many of the ROIs, but for the high recording only one curve (no. 13) where 20 ROIs is used have some similar features for both the low and high bpm recording. The mean value will always be between 0 and 255 because the recordings are uint8 images - 256 gray levels. Each ROI curve were assigned one color. It is also important to have in mind that these curves are not adjusted to remove trend spanning the recordings. This applies for all the figures. Not removing the trend was done because we primarily are interested to see the changes between to subsequent frames.

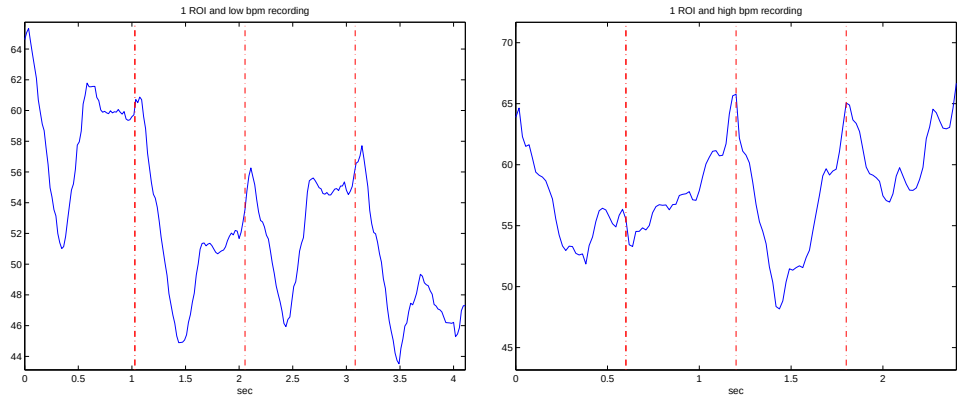

Figure 5.11: *The mean pixel intensity of 1 ROI for a low and high recording.*

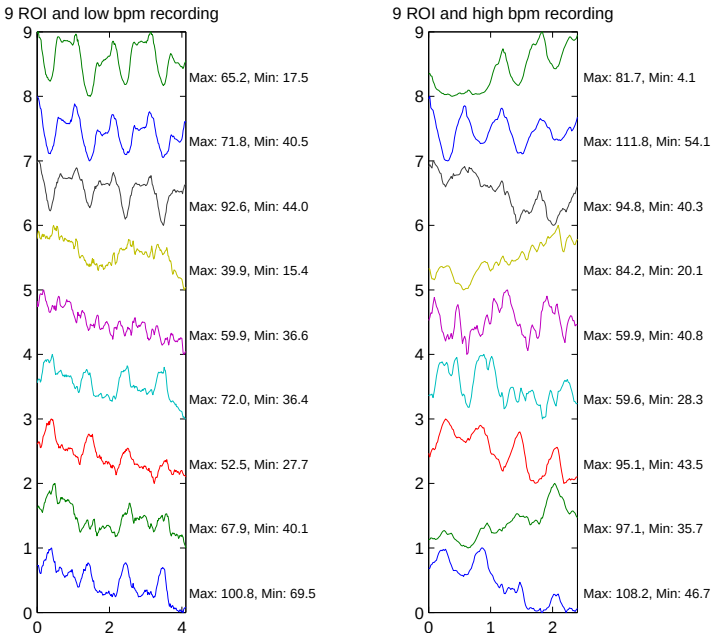

Figure 5.12: *Mean pixel intensity of 9 ROIs. Normalized between zero and one, and the real minimum and maximum values are at the side of each plot. The plots are of a low and high bpm respectively.*

5.4.2 Entropy

The results from calculating the entropy from 1, 9 and 20 ROIs are given in Figure 5.14 to 5.16. Also here the results are demonstrated with a low and high recording to see if there are some coincident patterns in the curves between the plots. Since the recordings are uint8 images, hence 256 graylevels and the entropy then never can be higher than 8, because $H_n(p_1, p_2, \cdots, p_n) \leq H_(\frac{1}{n}, \cdots, \frac{1}{n}) = \log_b(n)$. The curves are normalized between zero and one. The minimum and maximum value of the entropy in one ROI is written next to the curve in the figures. The figures show that the entropy always is between 2.2 and 7.7. When the entropy is high the image consist of many graylevels, and the histogram is uniform. For low entropy the image consist of few graylevels. Figure 5.14 with only one ROI shows that for a low bpm it got a pattern through the cardiac cycle. The same pattern was not to find in the acquisition for a high heart rate. For the 9 ROIs plot of entropy the same problem occur. It is possible to find some repetitive patterns for low bpm in some of the ROIs, but for the high bpm it is difficult. For the 20 ROIs there are some similarities for some of the ROI for both a high and low recording. Where these similarities are found the variation in entropy are not that high.

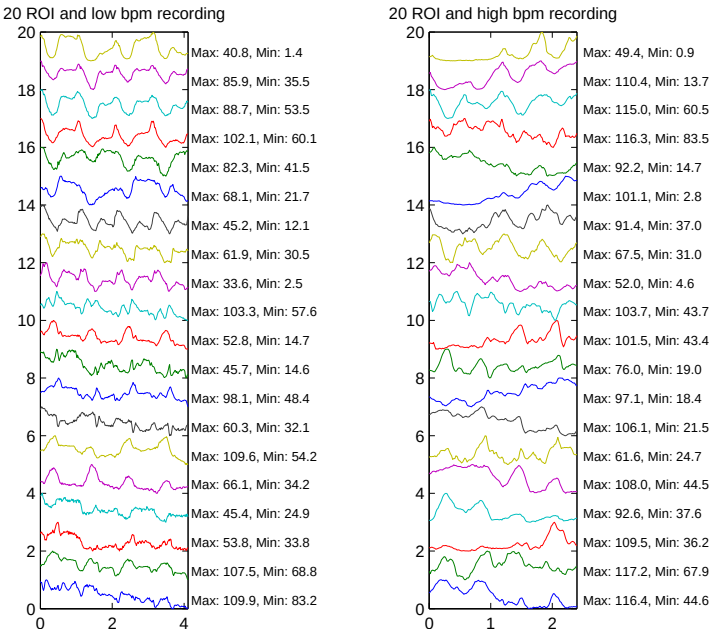

Figure 5.13: *Mean pixel intensity of 20 ROIs. Normalized between zero and one, and the real minimum and maximum values at the side of each plot. The plots are of a low and high bpm respectively.*

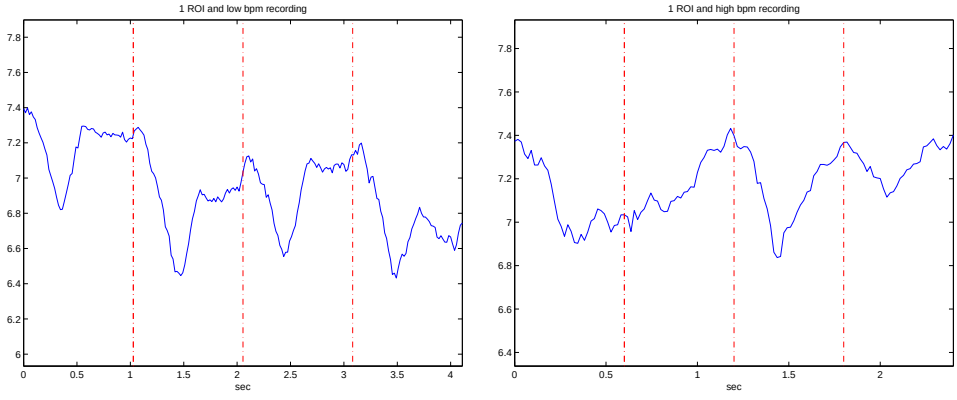

Figure 5.14: *Entropy of 1 ROI. The plots are of a low and high bpm respectively.*

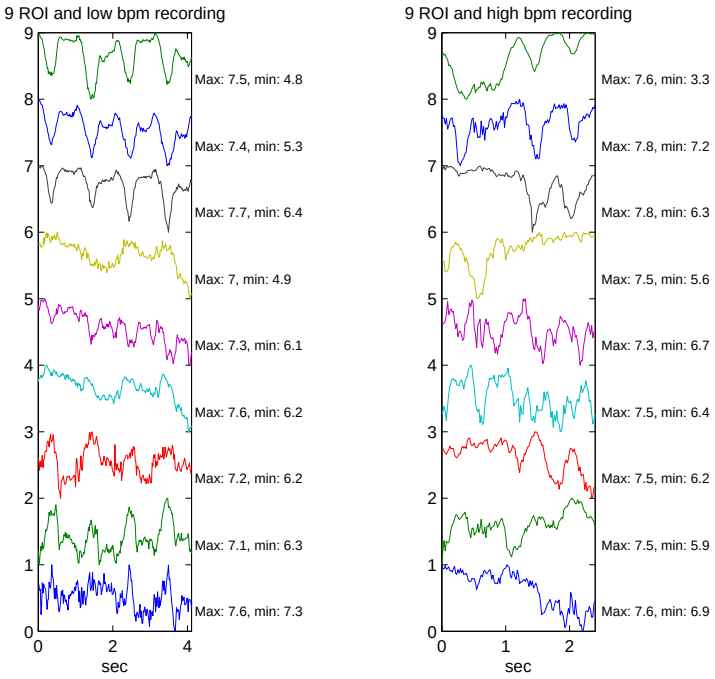

Figure 5.15: *Entropy 9 ROIs. Normalized between zero and one, and the real minimum and maximum entropy values are given in the plots. The plots are of a low and high bpm respectively.*

5.4.3 Mutual Information

The results from calculating the mutual information from 1, 9 and 20 ROIs are given in Figure 5.17 to 5.19. Also here the results are demonstrated with a low and high recording to see if there are some coincident patterns in the curves between the plots. Figure 5.17 shows mutual information of 1 ROI (global). It is possible to see some kind of pattern for the low recording, but the pattern for the high recording is not consistent. The same is to see in Figure 5.18 for 9 ROIs. For 20 ROIs it is also the same problem, but one or two ROIs for the high recording in the right plot in Figure 5.19 have a pattern similar to some of the low recording of the bpm. But this is not very convincing.

5.4.4 Earth movers distance

The results from calculating the mutual information from 1, 9 and 20 ROIs are given in Figure 5.20 to 5.22. Also here the results are demonstrated with a low and high recording to see if there is some coincident patterns in the curves between the plots. The result when comparing with only 1 ROI give us very little information. It is difficult to see some comparable pattern from the high and low curve. This is also the case when looking at 9 and 20 ROIs.

5.5 Discussion - histogram-based signatures

Neither of the three similarity analysis approaches give a clear significant pattern from one cardiac cycle to the other. For the low bpm recording it is for some ROIs possible to find a pattern, but when it is compared to the high bpm, the pattern and the features in the pattern is not possible to recognize. If it is difficult to find a repetitive pattern visually, we know that it also will be hard for a computer to do it. The big difference in the two recordings can have influenced the result to make it easier to find something that looked more similar and resemble a pattern. It is important to be aware of that for a too large number of ROIs, the calculation time increases and would make it more difficult, or impossible to make the algorithm run in real time.

Figure 5.11 to Figure 5.13 of the mean pixel intensity curve and Figure 5.14 to Figure 5.16 of the entropy curve of different numbers of ROIs look highly correlated. A possible explanation for the similarity of the curves can be found by looking at one of the frames in the ROI histograms used for calculating the entropy as seen in Figure 5.23. The histogram can be interpreted as an exponential function

$$p(I) = \begin{cases} \lambda e^{-\lambda I}, & (I \geq 0) \\ 0, & (I < 0). \end{cases} \tag{5.2}$$

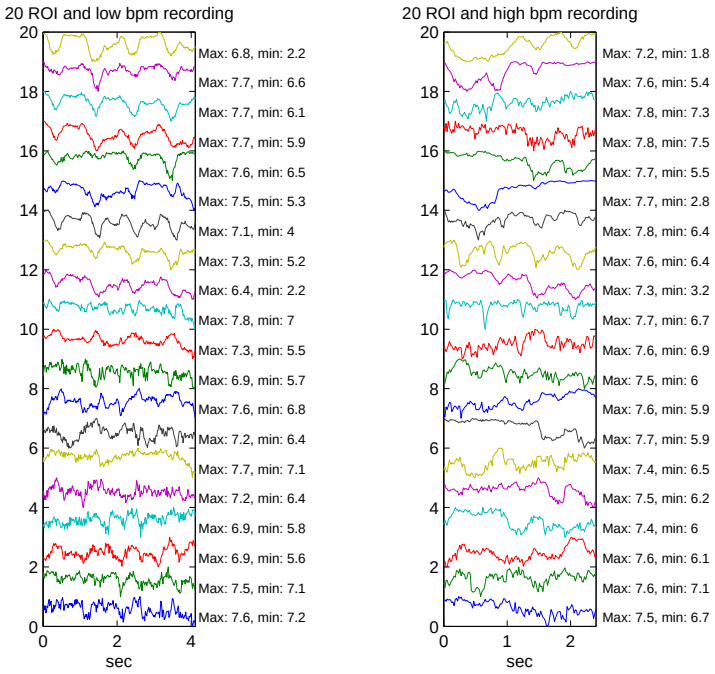

Figure 5.16: *Entropy 20 ROIs. Normalized to zero. The real entropy value is given in the plot.The plots are of a low and high bpm respectively.*

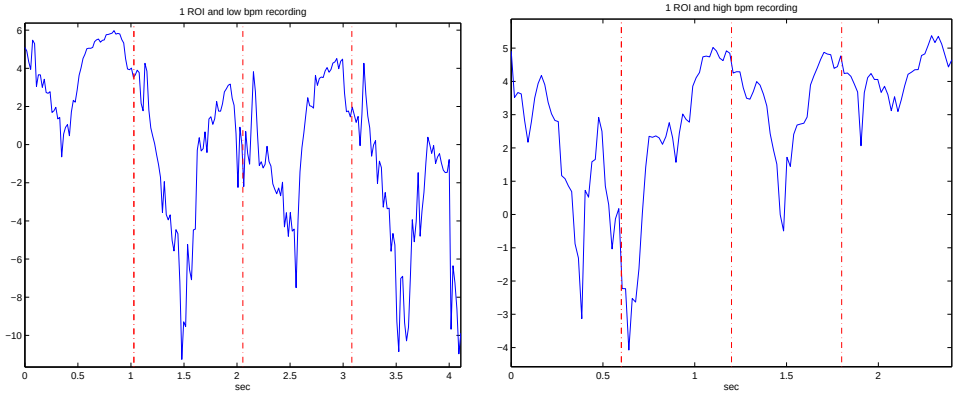

Figure 5.17: *Mutual information 1 ROI. The plots are of a low and high bpm respectively.*

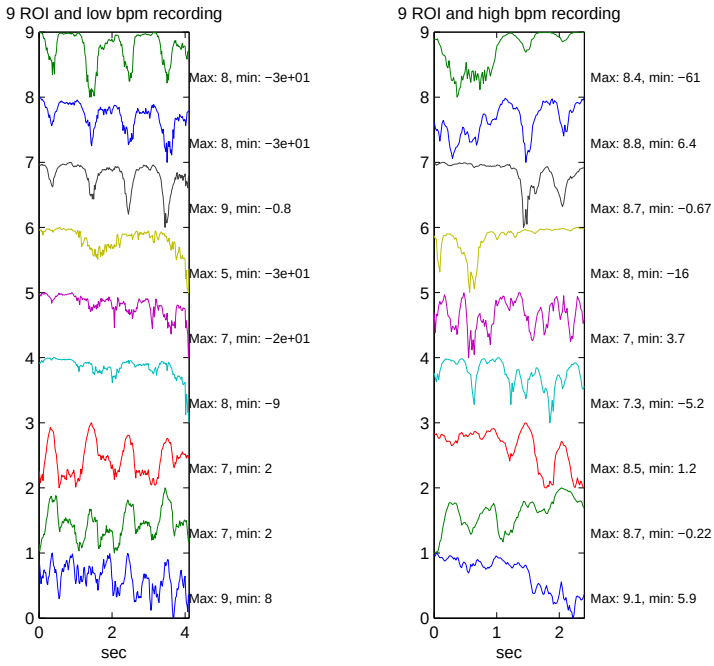

Figure 5.18: *Mutual information 9 ROIs, normalized to zeros, and the real minimum and maximum values at the side of each plot. The plots are of a low and high bpm respectively.*

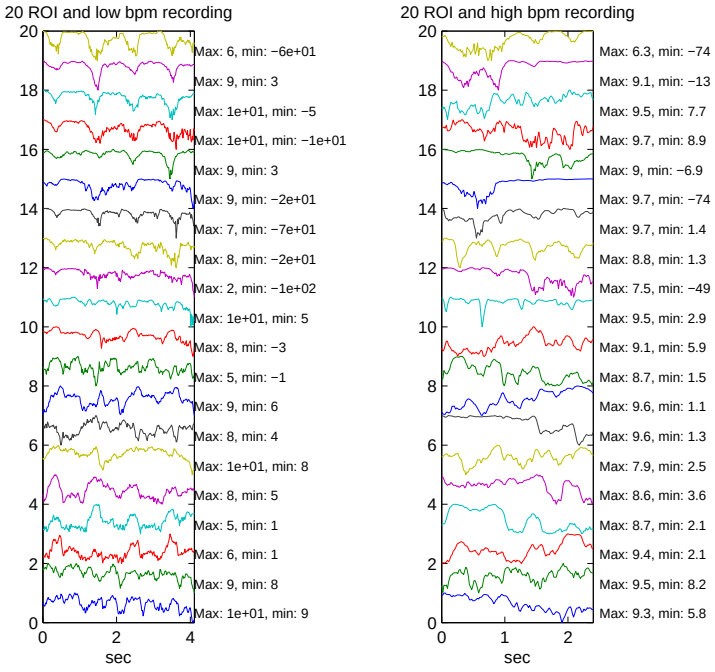

Figure 5.19: *Mutual information 20 ROIs, normalized to zeros, and the real minimum and maximum values at the side of each plot. The plots are of a low and high bpm respectively.*

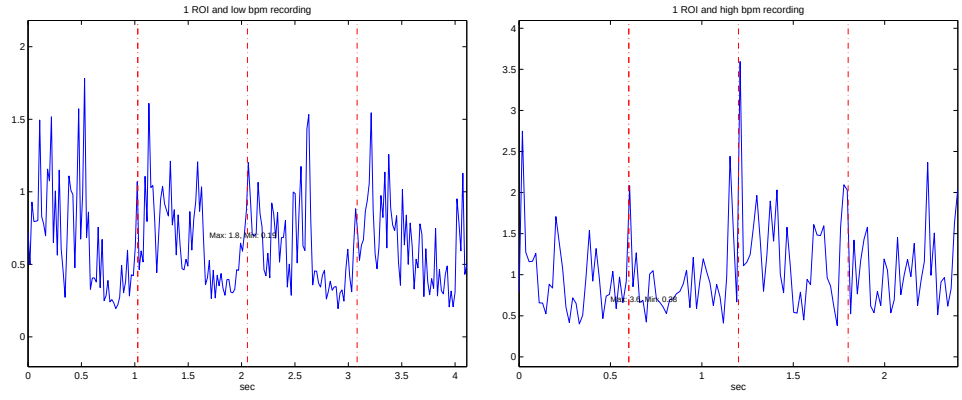

Figure 5.20: *Earth movers distance 1 ROI a normalized between one and zero, and the real minimum and maximum values at the side of each plot.*

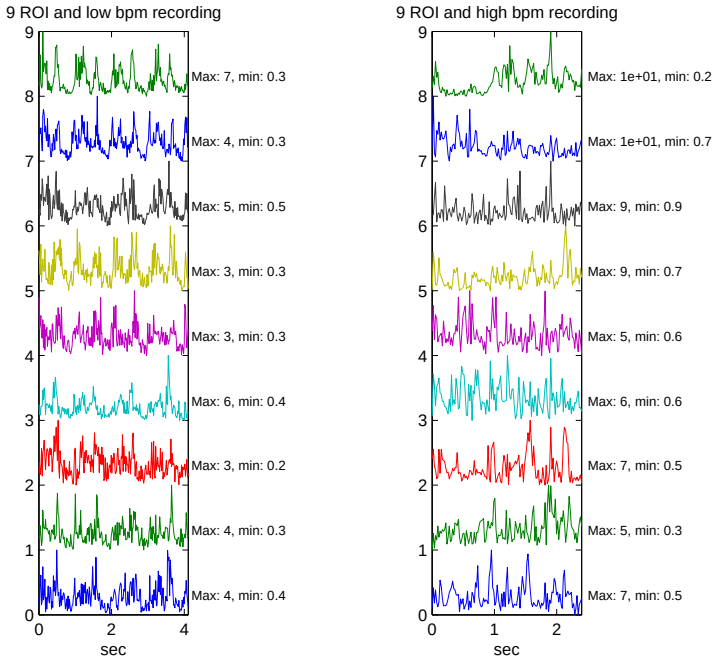

Figure 5.21: *Earth movers distance of 9 ROIs, normalized between one and zero, and the real minimum and maximum values at the side of each plot. The plots are of a low and high bpm respectively.*

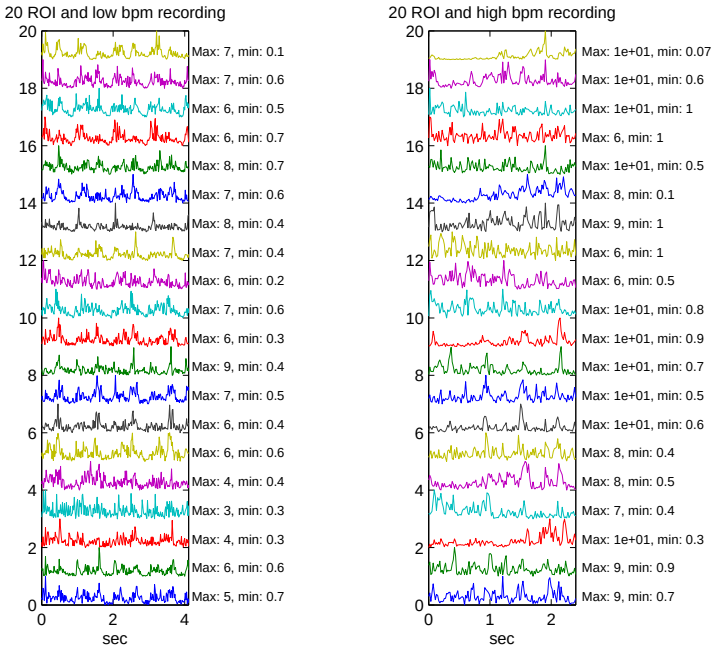

Figure 5.22: *Earth movers distance 20 ROIs, normalized between one and zero, and the real minimum and maximum values at the side of each plot. The plots are of a low and high bpm respectively.*

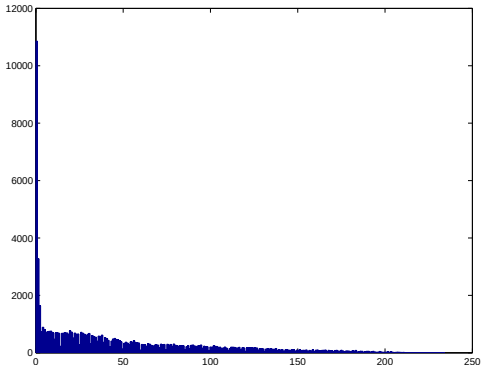

Figure 5.23: *One frame ROI histogram. The histogram show that there is a lot of pixels with the same pixel intensity.Thus, the histogram can be interpreted as exponential.*

The equation for entropy Eq.(2.11) can then be written as in the discrete domain

$$E = -\frac{1}{\ln 2}\sum_I p(I)\ln p(I), \tag{5.3}$$

$$= -\frac{1}{\ln 2}\sum_I p(I)(\ln\lambda - \lambda I), \tag{5.4}$$

$$= -\frac{\ln\lambda}{\ln 2}\sum_I p(I) + \frac{\lambda}{\ln 2}\sum_I p(I)\bar{I}, \tag{5.5}$$

$$= -\frac{\ln\lambda}{\ln 2} + \frac{\lambda}{\ln 2}\bar{I}, \tag{5.6}$$

where $\sum_I p(I) = 1$ and $-\frac{\ln\lambda}{\ln 2}$ is constant. We know that $\bar{I} = \lambda^{-1}$, therefore

$$E = -\frac{\ln\lambda}{\ln 2} + \frac{\lambda}{\ln 2}\frac{1}{\lambda}, \tag{5.7}$$

$$= \frac{\ln\bar{I}}{\ln 2} + \frac{1}{\ln 2}, \tag{5.8}$$

where $\ln\lambda = \ln\frac{1}{\bar{I}} = \ln\bar{I}^{-1} = -\ln\bar{I}$. Eq. (5.8) tells when the histogram has an exponential shape, there is a logarithmic relationship between the entropy and pixel intensity. This confirms the noticed resemblance between the mean pixel intensity curves and the entropy curves.

Chapter 6

Part I - Summary

6.1 Reconstruction, testing and extention of Aases algorithm

We saw that reconstructing Aases algorithm gave the same result as Aase got in his algorithm for detecting the cardiac cycle length. The result of using correlation as an alternative similarity measure also gave the same results as SAD.

There were many alternatives when choosing the number of ROIs. The challenge was to decide how many ROIs one should have in radial or azimuth direction. This depends on what one was looking for in the acquisition, for example radial movements or azimuthal movements. Many different alternatives were tested out, but there were no big differences when choosing to have more ROIs in radial rather than azimuthal directions. This is why only 1, 9, 20, 49 and 100 ROIs are discussed and shown in the report. As we saw from the results only one ROI would not work. The other chosen numbers of ROIs gave for many of the other tested parameters good results on the high and low data recordings. We also saw that differentiating the mean pixel intensity curve the algorithm made it more robust and that too much smoothing was not good. This was why we in the extended algorithm chose to use 9 and 20 ROIs. Larger numbers of ROIs would only make the algorithm run slower and would not increase the accuracy. Some smoothing would remove fast variations, so a 5th order smoothing filter was used. The same was used when reconstructing Aases algorithm.

The proposed extentions on Aases cardiac cycle length algorithm gave the same results as Aases algorithm, and at the same time removed the bmp limitations. There were no differences in the result when either SAD or correlation was used as similarity measure.

As mentioned in the small discussions earlier the big drawback of the testing and extention of Aases cycle length algorithm was the limited access to data recordings. This made it impossible to draw some real conclusions.

The only thing it proves is that it makes it possible to extend the algorithm on good acquisitions from one healthy male (me). :-)

6.2 Histogram-based approach

As seen from the three different histogram-based approaches, entropy, mutual information and earth movers distance, it was very difficult to find a similar and repetitive pattern between the low and high recordings. This could be because histogram-based methods uses the pixel intensities inside one ROI. If there was no sharp moving features inside the ROI, a repeated pattern would not occur, because the histograms are very different for one heart cycle to another. This was especially illustrated when the different methods were used on recordings of a high bpm. High recording gets bigger movements between two frames. Therefore the histogram information also can be very different between a low and a high bpm recording. Also the angle and brightness on the acquisitions will influence the histograms. The data recordings used in the histogram-based approach had been filtered to remove speckle and sharper edges. This should be an advantage for this approach. If we had sharper edges inside one ROI and the ROIs had been covering important features the method might have worked.

From the analysis we found that the histogram-based methods based on pixel intensity do not give a curve that could hold features for both a low and high bpm recording in the same way as the ECG curve.

Based on the discussion of the histogram based approaches an alternative approach that is based on the movements between the frames and not the changes in the pixels graylevel intensity is proposed in the following.

Chapter 7

Part II - Method

Optical Flow

The results from using histogram based methods did not give any curves with repetitive pattern for both a high and low bpm recording that could be used as a general "substitute" or complement to the ECG curve. Therefore a new approach was tested, optical flow; Optical flow looks at the pixel movement in-between subsequent frames, whereas histogram based methods look at the pixel distribution in one frame or between two frames.
We start by implementing Lucas & Kanades and Farnebäcks optical flow algorithms. The algorithms are then run on the recorded ultrasound acquisitions. Then features from the flow vectors generated will be used try to find a repetitive pattern in the recorded ultrasound data.

7.1 Implementing the Lucas Kanade and Farnebäck algorithms

The .h5 file format containing the ultrasound recordings and corresponding ECG signal were used. These files had to be scan converted before further data processing could be done. The images were scan converted to Cartesian coordinates by using bi-linear interpolation in Matlab [MathWorks, 2013].

7.2 Lucas & Kanade algorithm

Matlab was used for implementing the Lucas & Kanade algorithm as described in Chapter 2.7.3. This implementation required different parameters that were tested with different values to find the optimal set of parameters; Window sizes of 3 and 5 pixels in x and y direction, number of pyramid levels between 1 and 3, and number of iteration between 1 and 3. The final parameter values were chosen to be; Window size of 5×5 pixels, 1 pyramid

level and 3 iterations. The algorithm was set up to go through all the frames in the recorded ultrasound scan and finding the optical flow between two and two subsequent frames.

7.3 Farnebäcks algorithm

Farnebäcks algorithm was downloaded from OpenCV[1]. This is a python implementation, so the script was run in python. The algorithm works as described in Chapter 2.7.4. The scan converted ultrasound recordings were dumped as a uint8 file from Matlab in order to be used in Farnebäcks OpenCV algorithm. Farneback algorithm needs different parameter values, so different values were tested for numbers of iterations (1-5), pyramid levels (1-3), neighborhood values (5-7) and window size (3-15). The pyramid scaling factor were set to 0.5. i.e. downsizing of the image to half the image size for each level. The parameter values were set to extreme values to easier show how they affected the optical flow calculation. The final parameters used were: Numbers of iterations 3, pyramid levels 2, neighborhood values 5 and window size 5. The standard deviation was set to 1.1. Farnebäcks algorithm was run through all the frames calculating the optical flow between to subsequent frames. It was plotted with flow arrows, to give a visual impression of the flow. The optical flow results were saved as two 3-dimensional matrices, one for the x-coordinates of the flow vectors for each optical flow frame, and one for the y-coordinates for each optical flow frame. This was then dumped back to Matlab for further data processing.

7.4 Angles, length and variance of the flow vectors

The properties of the vector field seen in Figure 2.7 processed by Farnebäck's algorithm, were from each frame and ROI reduced to a few 1D features. What we wanted to do was:

- Find a repetitive pattern from the flow vectors.
- See if it was essential to divide the flow vectors into ROIs, so we could capture movement of the heart in horizontal and vertical direction.
- See if this method worked for different heart rates.
- If we got a repetitive pattern of the mechanical movement of the heart, then compare and match it to the ECG pattern and features in the heart cycle, such as the closure of the mitral valve.

[1]OpenCV is a library of programming functions for real time computer vision [Bradski, 2000].

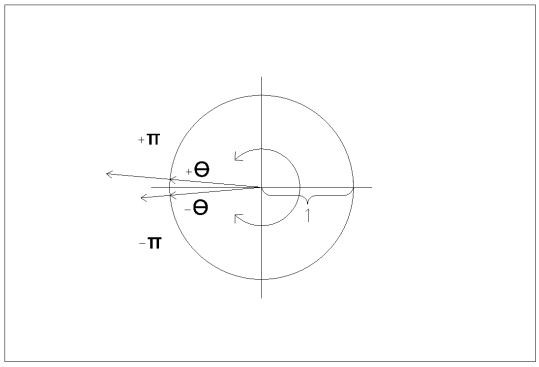

Figure 7.1: *Figure displaying how the wrapping error occur.*

- The systole and diastole pattern of the blood pressure were explored as seen in Figure 2.6.

To find the repetitive pattern we first looked at the lengths and angles of the flow vectors. We wanted to reduce all the information in one ROI to one feature. This was done testing the following steps in the pseudo code below:

Algorithm 2

for all number of ROI **do**
  for all optic flow frames **do**
    calculate length of all flow vectors, l_i
    calculate the mean of the lengths, $\bar{l}$
    calculate the variance of the lengths, Var(l)
    calculate angles of all flow vectors, θ_i
    calculate the mean of the angles, $\bar{\theta}$
    calculate the variance of the angles, Var(θ)
  end for
end for

When the angles and lengths were found, a function of angels and lengths versus time/frame were plotted. The calculation of the flow vectors were done on images that were laterally flipped, compared to how it normally are presented on scanners. The "variance" Var $\hat{\theta}(t)$ that first was calculated in Algorithm 2 may contain wrapping errors, i.e. discrete jumps with height 2π. For the calculation of $\bar{\theta}$ we therefore had to be aware that angles wrap around π (180°) to $-\pi$ (−180°). As an example the mean of 175° and −175° is not 0 but 180° as seen in Figure 7.1. The calculations of $\bar{\theta}$ was therefore done by normalizing all vectors to length equal 1. Then the mean of the imaginary part (y-componet) and real part (x-component) was found separately. $\bar{\theta}$ was

calculated as

$$\bar{\theta} = \arctan\left(\frac{\text{imaginary part}}{\text{real part}}\right). \tag{7.1}$$

The variance to $\bar{\theta}$ was estimated by the standard formula,

$$Var(\theta) = \frac{1}{n}\sum_{i=1}^{n}(\theta_i - \bar{\theta})^2, \tag{7.2}$$

where n is the numbers of angles in the ROI. By adding 2π to the values from the calculated mean values of the angles that were between 0 and -2π we tried to remove the wrapping artifacts that still could accrue between consecutive time samples.
The "variance" containing the wrapping errors where calculated in the same way as in Eq. (7.2), but $\bar{\theta}$ was repaced with $\hat{\theta}$ which was not adjusted to avoid wrapping artifacts that means that $\hat{\theta}$ was calculated as

$$Var(\hat{\theta}) = \frac{1}{N}\sum_{i=1}^{N}\arctan\left(\frac{\text{imaginary part}_i}{\text{real part}_i}\right). \tag{7.3}$$

7.4.1 Testing out ROIs

With the same number of ROIs; 1, 9 and 20, as used in the histogram-based methods in Part I, we want see if it is possible to find some patterns in the ROIs. This was done by dividing the acquisition for both a high and low bpm ultrasound recording into ROIs in the same way as described in Chapter 4.1.

7.4.2 Removing clutter

An attempt to remove potential clutter was implemented as exclusion of the vectors that were smaller than $a \times \bar{l}$, where $a \in [0, \ldots, 1]$. and $\bar{l}$ the mean of the length of the flow vectors. This was done thoughout the time series of optical flow frames. Different values of a was tested.

7.4.3 Comparing the optical flow and ECG curve

The ECG curve retrieved from the .h5 file was plotted in the same plot as the optical flow curve. This was to compare the optical flow pattern with the ECG curve and see if there were some similarities and equal events.

7.4.4 Testing optical flow algorithm on several subjects

The data sets with different bpm recordings from the different subjects were tested using the optical flow algorithm. This gave a pattern of the optical flow depending on the bpm in the recording. The ECG curve was plotted in

the same plot as the optical flow curve to compare the flow pattern with the events in the ECG curve.

7.4.5 Finding events in the optical flow pattern

By manually finding the opening and closing of the mitral valve, the tricuspital valve and the aorta valve in the ultrasound acquisition, these events could be plotted together with the optical flow curve and the ECG curve. This was to see if there was any coincidence between the events in the optical flow curve and the opening and closing of the valves. The quality of the ultrasound recording was also reviewed so we could discuss how easy it was to detect the different valve events. In a poor acquisition the events are more difficult or impossible to detect.

7.4.6 Optical flow curve vs blood pressure curve

A comparison with the blood pressure curves from Figure 2.6 were also done. This was done manually by looking at the similarities in the angle variance curve and the blood pressure curve.

Chapter 8

Part II - Results and Discussion

Optical flow

In this part the results of applying optical flow to the ultrasound recordings are displayed, commented and discussed.

8.1 Lucas & Kanade or Farnebäcks optical flow algorithm

My Matlab implementation of Lucas & Kanades algorithm was very slow. There was also some uncertainty regarding the verification of the algorithm and interpretation of the result from Lucas & Kanade. Farnebäcks OpenCV algorithm on optical flow was implemented parallel with the Lucas & Kanade implementation. The Farnebäck algorithm is known to be both quick and accurate [Farnebäck, 2002]. The implementation of the Farnebäck algorithm immediately gave good results, and more importantly was a lot faster than my dense Lucas & Kanade implementation. The choice was therefore made that further work would be done using Farnebäcks openCV algorithm.

The results received from optical flow calculation between to frames are always given in two 2D matrices. One for the $x - coordinates$ and one for the $y - coordinates$ of the vectors.

8.2 Calculation of the length and angles of the flow vectors

The results of calculating the length and angles of the optical flow vectors obtained by Farnebäcks optical flow algorithm, are shown in Figure 8.1. The

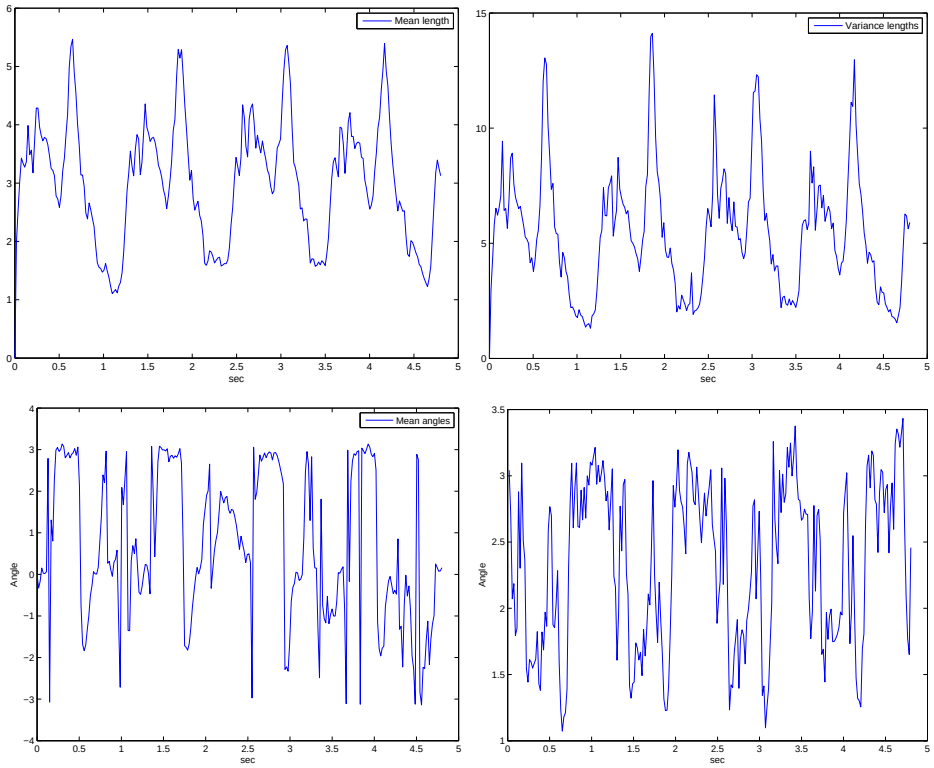

Figure 8.1: *The upper left plot displays the mean of the length curve in the optical flow vectors in one ROI. The upper right plot shows the variance of the length curve for optical flow. The bottom left plot shows the mean of angles curve. The bottom right plot shows the variance of angles curve. All the plots are from a low bpm recording.*

results in these four plots show that it is possible to find a repetitive pattern for a low bpm recording. The two upper plots contain the curves of the calculated mean of the lengths, and the calculated variance of the lengths for one ROI. The two bottom plots are the mean of the angles and the variance of the angles. In the bottom left plot we see that the curve often jumps from a value close to π to a value close to $-\pi$. In the bottom right plot of the variance of the angles we see that the jumps from a value close to π to a value close to $-\pi$ disappears. We see that the expected value of the variance is positive.

8.3 Discussion - Length and angles of the flow vectors

Figure 8.1 shows the length and angle of the estimated optical flow together with the variance of these measures for one of the test persons. As seen in the figure, the four plots show distinct patterns and features in each of the four cardiac cycles. It was therefore interesting to do further analysis of the results obtained with the optical flow method, starting with the estimated mean and variance of the angles.

8.3.1 Mean and variance of angles

In Figure 8.2 the mean flow vector angle for the two first cardiac cycles are displayed together with a curve that shows if the mean angle is of positive or negative value. From Figure 8.2 we see at for example at 0.2 second a discrete jump from a value close to π and to a value close to $-\pi$. (In Chapter 7.4 the problem of discrete jumps between π and $-\pi$ was explained.) Figure 8.3 displays the curve when the angles are plotted between 0 and 2π. Compared to the curve in Figure 8.2, this curve has more wrap-around errors. At the same time it is not that easy to see any specific pattern in this curve. From this simple exercise it was concluded that it would not be very easy to convert plots of mean angle into a stable and reproducible curve that could act as a mechanical ECG.

The variance of the angles shown in the lower left part of Figure 8.1 does show a repetitive pattern, but the curve lacks a distinct feature, for instant a high spike or a deep null, occurring in every heart beat that could act as a marker or a signature. It does have several minimum points, but it is hard to distinguish one from the other within a heart beat. On the positive side is that the variance does not show wrap-around errors.

8.3.2 The non-adjusted angle variance

Alone, the two curves discussed above do not seem to fulfill the requirement of being a mechanical ECG curve. But a combination of the information in the two curves could do the job. This because at the beginning of the heart beat, the mean angle is constant and close to π while the variance is relatively low. Later in the heartbeat, the mean angle is close to zero while the variance is relatively high.

When using optical flow on ultrasound images of the heart it is important to be aware that there is a relation between the direction of the flow and where the probe is placed. When the heart moves away from the probe the flow vectors will point in a direction away from the probe, and the mean angle will in our case be close to π.

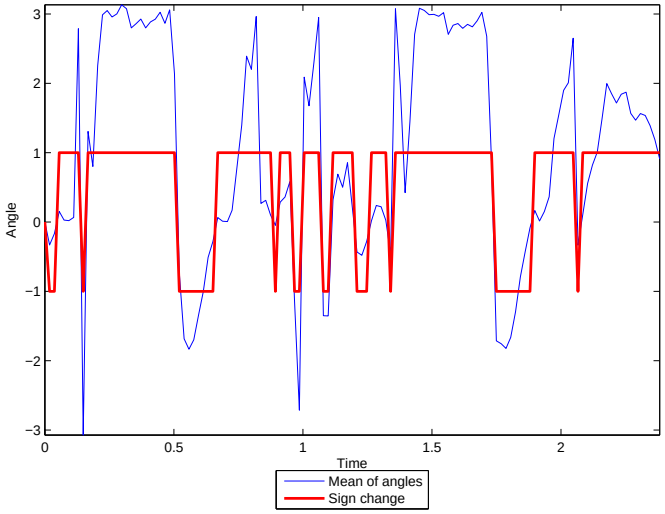

Figure 8.2: *The figure displays the mean of the angles with the sign shift for two cardiac cycles.*

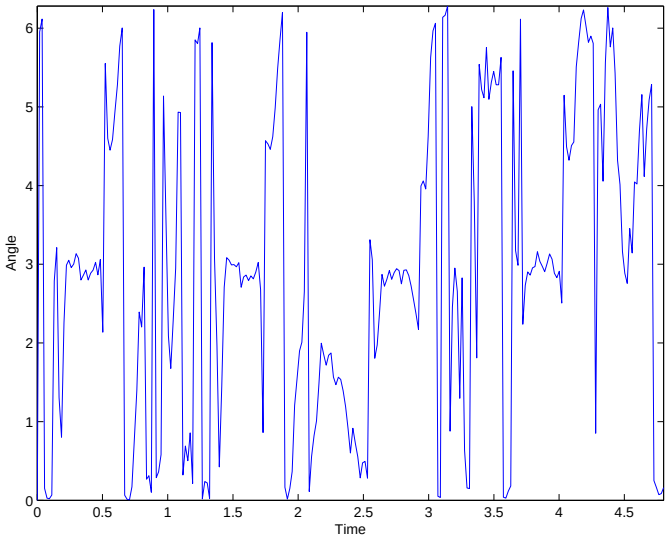

Figure 8.3: *The plot shows how the mean angle curve looks when adding* 2π *to the negative angles.*

When then taking into consideration the problem described and illustrated about angles around π and $-\pi$. in Chapter 7.4 it might be possible to use this wrapping error as an advantage instead of a problem. If the true mean value given by Eq. (7.2) is close to π and the optical flow vectors are quite homogeneous, a histogram of all angles will look something like the left plot in Figure 8.5. The mean calculated with Eq. (7.3) would in this case be close to zero. An alternative variance measure calculated with the mean given by Eq. (7.3) would then be high. In the opposite case, where both Eq. (7.2) and Eq. (7.3) gives a mean close to zero, the histogram would look something like the right plot in Figure 8.5 and the variance would be relatively low and equal in the two cases.

Figure 8.4 shows plots of the angle variance when using Eq. (7.2) or Eq. (7.3) as a estimate for the mean. The true, or correctly, estimated variance is here called "Angle variance adjusted for wrapping errors", while the one with the wrong mean estimate is called the "non-adjusted angular variance".

As seen from the figure, the non-adjusted angle variance does show a repetitive pattern, it has a distinct feature since it seems to become high early in every heartbeat. The curve does combine the information of the mean angle and angle variance in a clever way resulting in one, and not two curves.

When looking at an ultrasound image of a heart, you can see that the there are a lot of different movements. The events that make the heart have a distinct movement can only be speculated about. My speculations are either that when the electrical impulse from the sinus node make the heart beat, there are some rapid and homogenius movements in the heart in the direction. Another speculation can be that the valve movements contribute to the direction in the image. The wrap-around error occurs when the valves are opening and closing, which can be seen by manually inspection the ultrasound recordings. Figure 8.4 shows the angle variance in two different coordinate systems. The thick blue curve is where we first find the mean of the angles and then use that value as the zero angle to calculate the variance. This was also explained in Chapter 7.4. The thin dashed red line is of the variance we get by not rotating the coordinate system such that the positive x-axis coincides with the mean angle. The wrap-around error of the thin dashed red curve is not pressent in the blue curve.

8.3.3 Mean and variance optical flow vector curve

From the plot in Figure 8.6 we see that the mean and variance curves of the lengths of the optical flow vectors are quite correlated. They actually have a correlation coefficient at 0.965. This is also confirmed by the scatterplot in Figure 8.7. When the movement is small in the heart, the flow vectors also are small, when the movements are larger, the variance also is higher. This also seems logical when looking at the flow vectors between the ultrasound

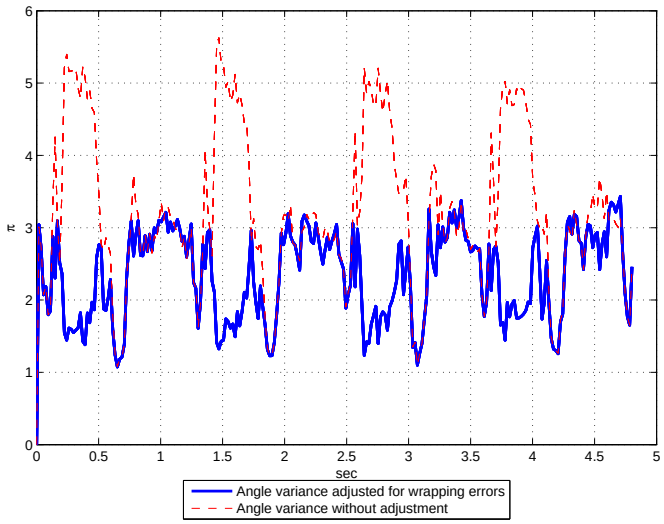

Figure 8.4: *The plot shows how the variance curve changes from when adjusting for wrapping errors.*

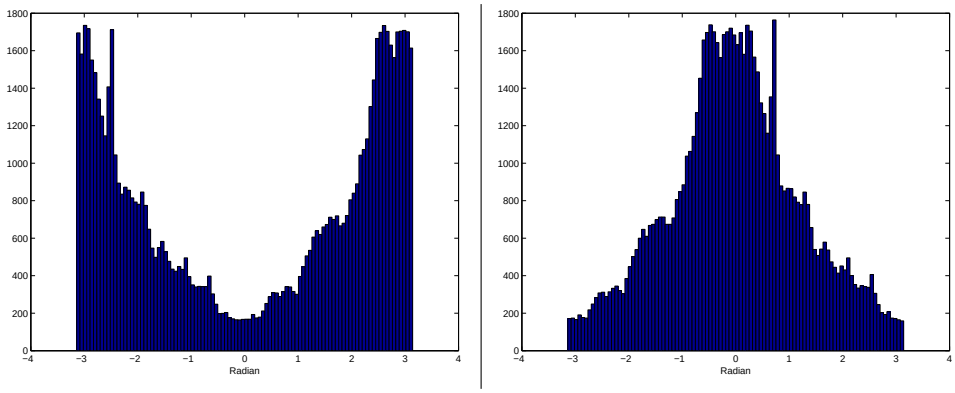

Figure 8.5: *The left histogram displays the distribution of the angles when they are not adjusted, right histogram are of adjusted angles.*

frames. The curve of the non-adjusted angular variance is also plotted in Figure 8.6. A difference between the two length curves, looks to be that the strongest features get more highlighted in the variance of lengths curve. The figure also show that there is a relation between the maximum values of the length curves for each cardiac cycle and the minimum value of the non adjusted variance curve for each cardiac cycle. We therefore chose to do further comparison, analysis and testing on the non adjusted variance of the angle curves. This curve seems to have more features than the mean and variance length curves because it will be more difficult to separate all the peaks in the mean and variance of the length curves within one cardiac cycle. We also have shown that if we decide to use the length, we only would need one of them due to the high correlation.

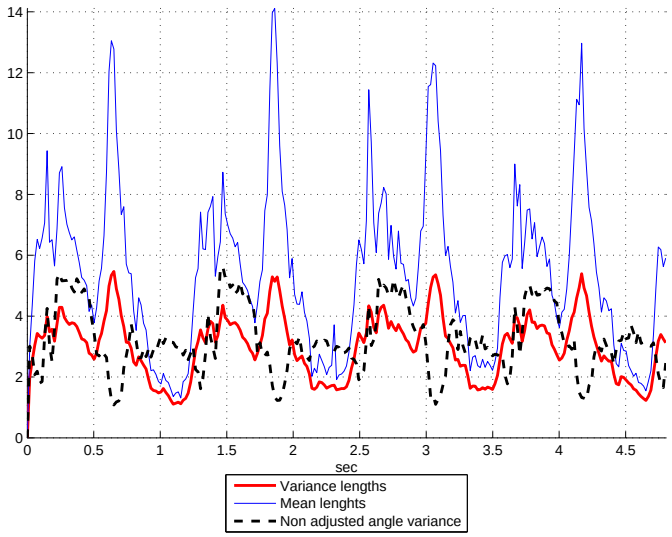

Figure 8.6: *The figure displays the mean and variance of the length of the optical flow vectors. They are compared to the non adjusted angel variance curve.*

8.4 Testing different attributes

Below are the results of testing different parameters for the optical flow algorithm and reasoning for decisions made for further work with the non-adjusted variance of the angle curve.

8.4.1 Parameter choices

As mentioned in chapter 7.3, in Farnebäcks OpenCV algorithm we have to set different parameters. Figure 8.8 displays how the different parameters

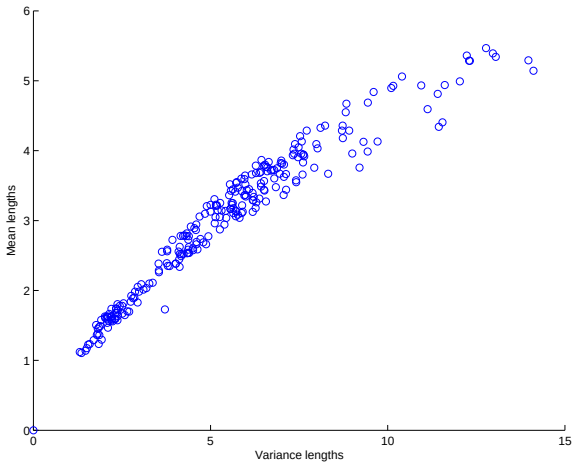

Figure 8.7: *The figure displays a scatterplot between the variance and mean of the length of the optical flow vectors. The correlation coefficient between the two vectors is calculated to be 0.965.*

affect the form of the curves for the different parameter values. The different parameter values used in the optical flow algorithm was set to what was assumed to be the outer boundaries. As the plot shows there was not so much difference between the choice of the different parameters within the curves. The blue thick line is of the parameters that we ended up using. These parameters were chosen because the curve looked like an average of all the curves. The curves also displays that the algorithm is robust, this also supported the decision to use parameters chosen.

8.4.2 Number of ROIs

When testing out the histogram based methods and the mean pixel intensity described in the Aase algorithm, different numbers of ROIs were used. Figures 8.9 to Figure 8.11 show how the number of ROIs affects the results for the optical flow algorithm. Both the high and low bpm recording results are presented to show the similarities between the curves. They have some of the same features even when the heart rate was increased. From the different calculation we see that the result using only one ROI gives a very good curve. We actually see that when using more ROIs it is only the lower regions where we really find the same curve as the one we get when using only one ROI. It would therefore be easier to use only one ROI. In that way we do not have to concern about the challenges you get to choose only a few of the curves or a combination of them.

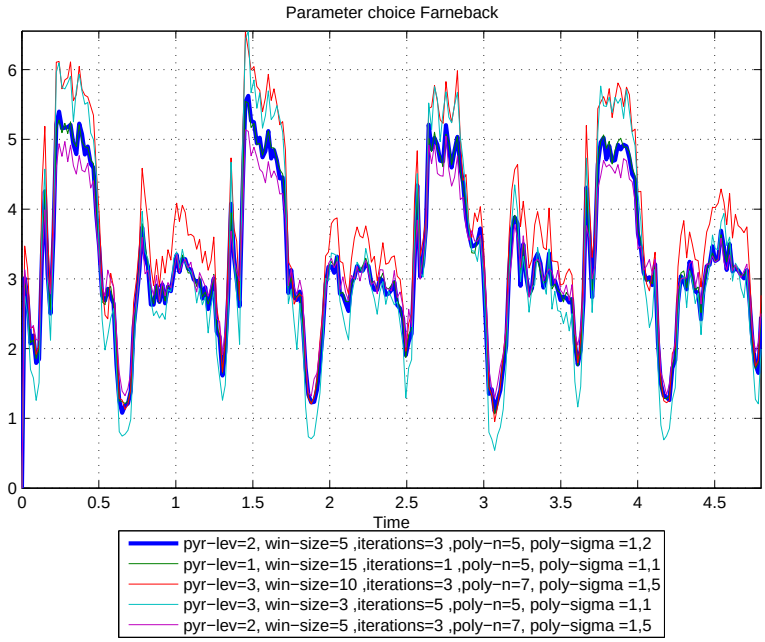

Figure 8.8: *The figure show how different choices of parameters for Farnebäcks optical flow algorithm implemented in OpenCV affects the result of the angles variance plot. The thick blue line is of the parameters that were selected.*

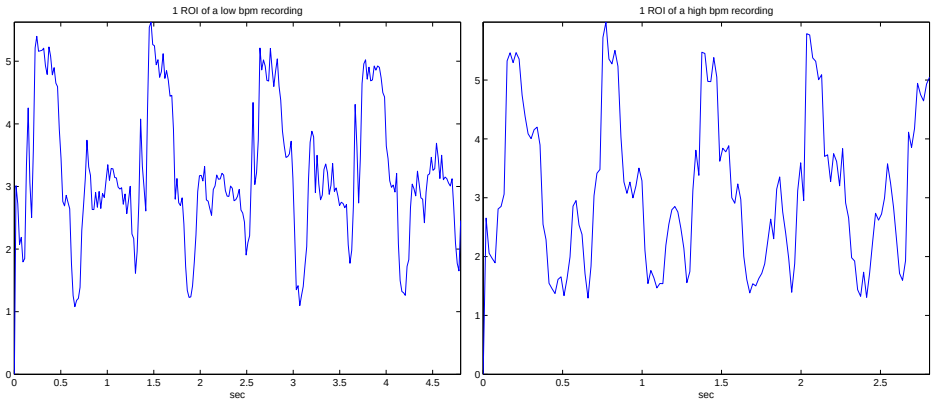

Figure 8.9: *The figure displays the angle variance of calculated optical flow vectors of 1 ROI for a low and high bpm recording.*

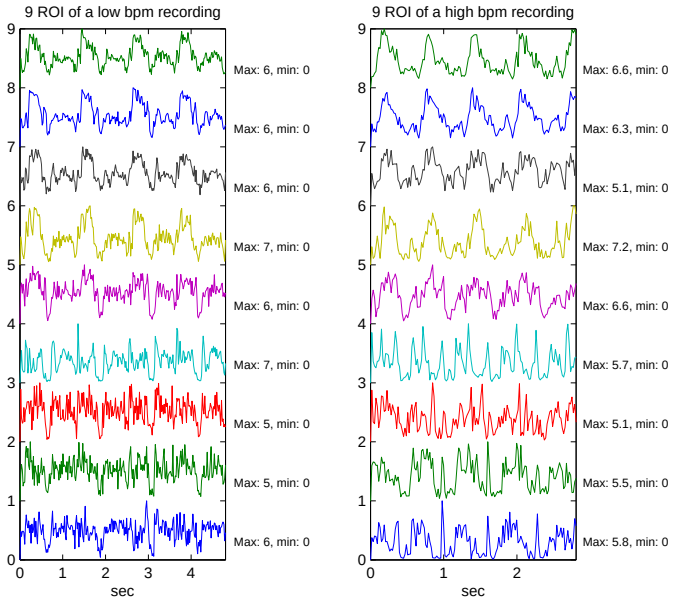

Figure 8.10: *The figure displays the angle variance of calculated optical flow vectors for 9 ROI. The curves are normalized between zero and one and plotted starting with the upper left ROI at the bottom of the figure and then its adjacent right ROI as the curve second form the bottom.*

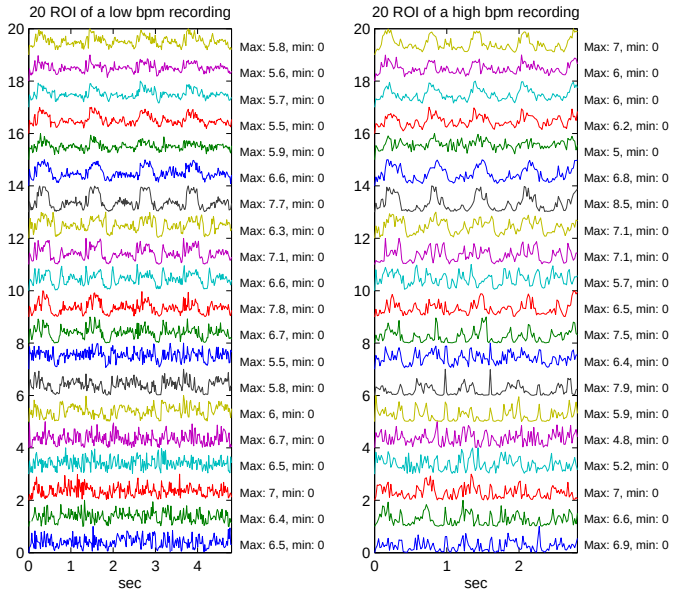

Figure 8.11: *The figure displays the angle variance of calculated optical flow vectors for 20 ROIs. The curves are normalized between zeros and one and plotted starting with the upper left ROI at the bottom of the figure and then its adjacent right ROI as the curve second form the bottom.*

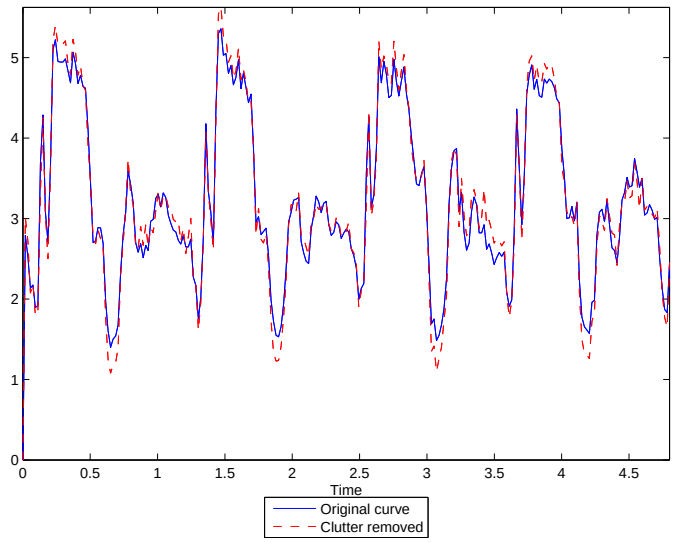

Figure 8.12: *The figure displays how removal of the short vectors affects the curve of angle variance curve.*

8.4.3 Removing clutter

In images, clutter will be shown as a uniform shadow that does not move together with the other structures. The movement of this shadow will typically be less than the actual movements of the heart. Figure 8.12 displays how the non-adjusted angular variance curve were affected when all short vectors were removed. It is plotted together with the original non-adjusted angular variance curve. As seen from the curve, removal of the short vectors does not affect the curve much. The main difference is that the minimum value becomes lower; and therefore creates a more distinct dip in each cardiac cycle. The rest of the presented results are done on data where the clutter was supposed to be removed. Because we do not know exactly the length of the clutter vectors we looked at the distribution of the vectors and chose $a = 0.5$ as described in Chapter 7.4.2

8.5 Comparing optical flow and ECG curves

The non-adjusted angle variance was plotted together with the ECG curve to see if they had some similar features. This was done on low and high recordings on all four subjects. The results for 2 subjects are shown since they were all very similar. As we can see from Figure 8.13 to Figure 8.15 where the non-adjusted angle variance is plotted in blue and the ECG curve are plotted in red, the R and S waves which was described in Chapter 2.2.4, seem to occur almost at the same points as the non-adjusted angle variance

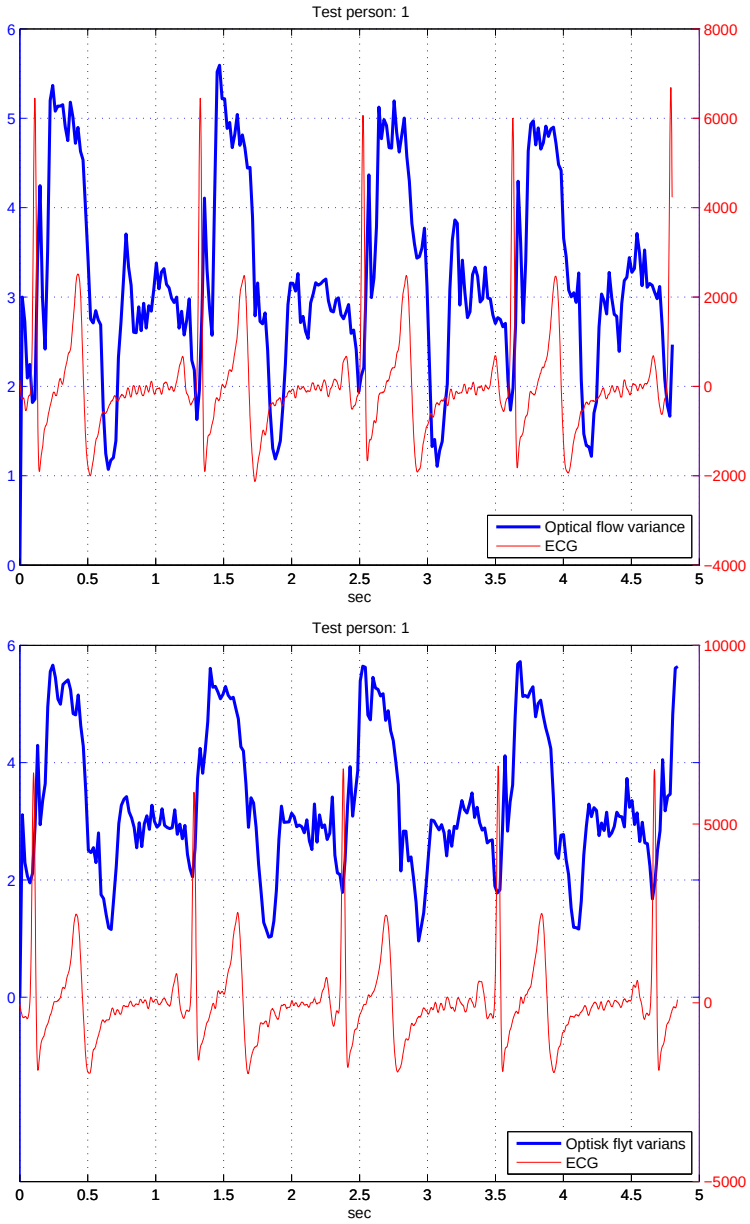

Figure 8.13: *The top plot is of an apical four-chamber scan, the bottom plot an apical long-axial scan form test person one. Both compared with the ECG trace. The plots are of a low bpm recording.*

attain a minimum before it becomes large for a longer period. It is very easy to see this relationship in the two fist plots in Figure 8.13 of test person 1. This seems to be a distinct similarity feature between the two curves. This relationship can also be studied in .avi files available at my home page

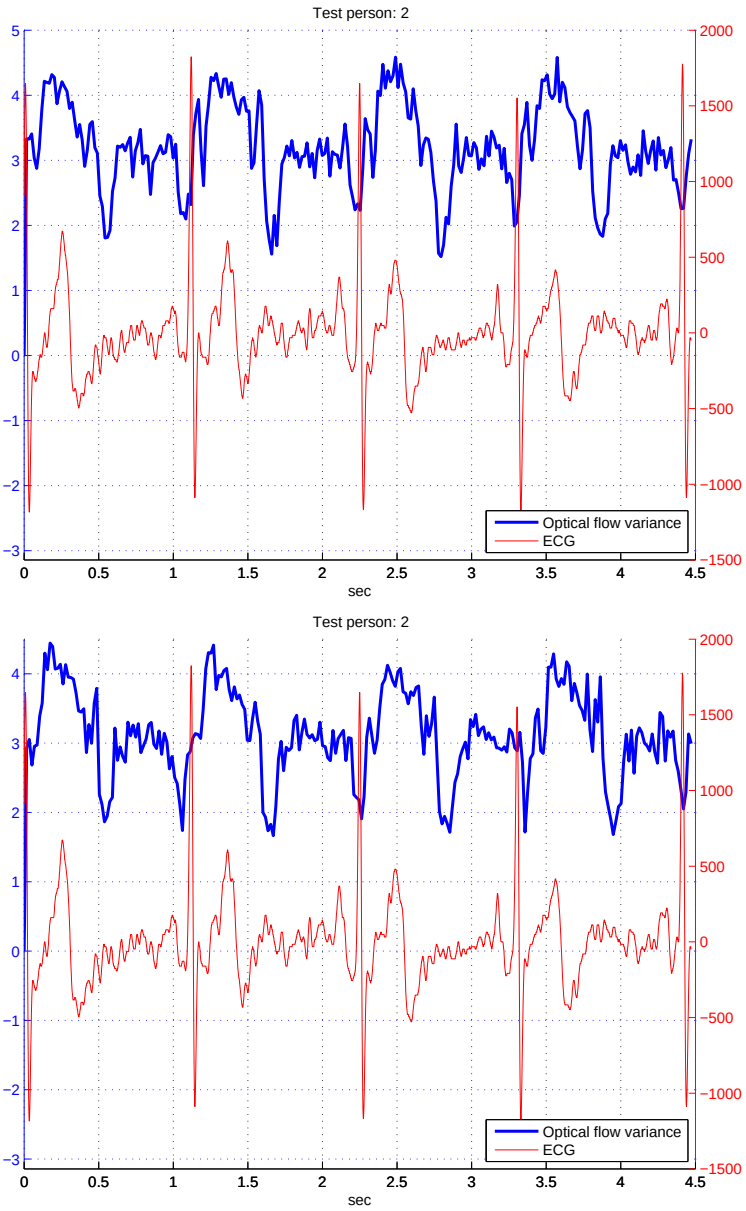

Figure 8.14: *The top plot is of an apical four-chamber scan, the bottom plot an apical long-axial scan form test person two. Both compared with the ECG trace. The plots are of a low bpm recording.*

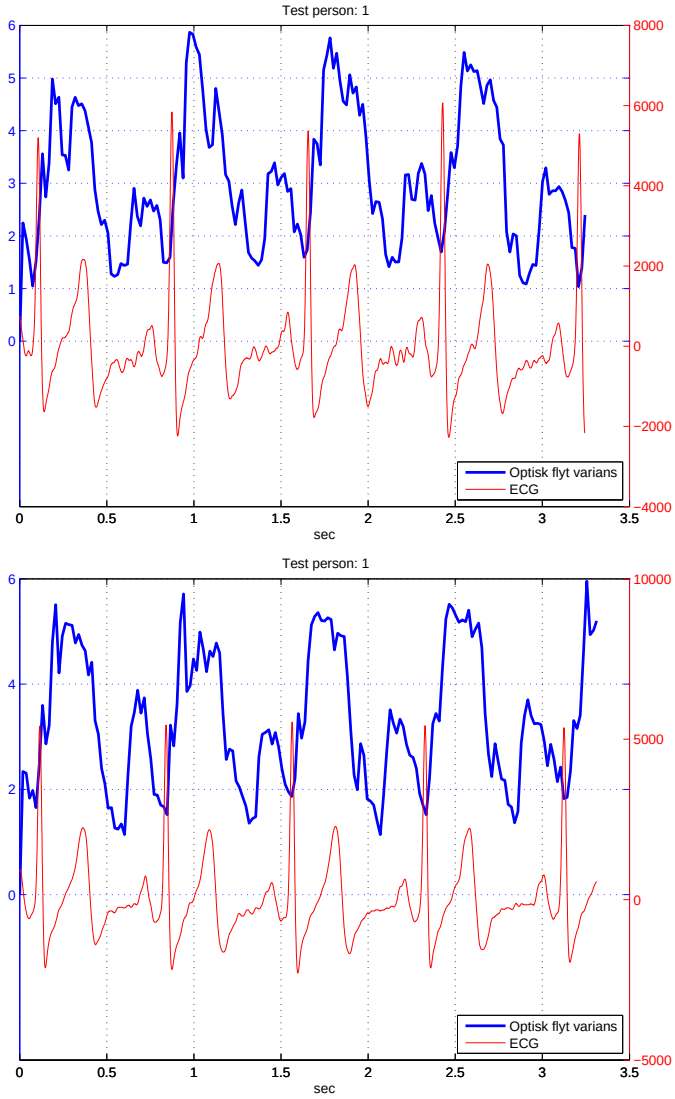

Figure 8.15: *The top plot is an optic flow variance estimation of an apical four-chamber scan and the corresponding ECG. The bottom plot is of an apical long-axial scan and the corresponding ECG. Both plots are of a high bpm acquisition.*

at *folk.uio.no/jacobln*. We also see that the non-adjusted angular variance curve have other events that maybe can extract other features of the hearts movement. The optical flow curve is calculated on the basis of apical four-chamber scans in the first plots Figure 8.13 and Figure 8.14, and apical long-axial scans in the second plots in the respective figures, these are all of low bpm recordings. In Figure 8.15 they are of high bpm recordings.

8.6 Finding valve events

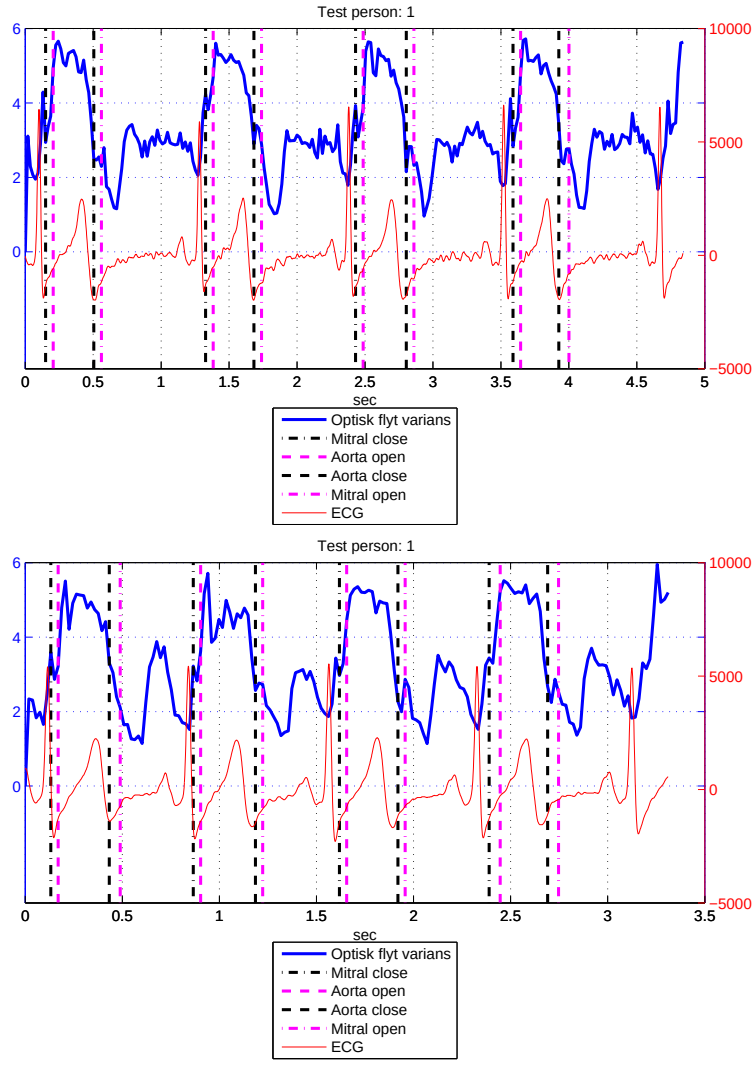

Figure 8.16: *The top plot is an optic flow variance estimation of an apical long axis scan and the corresponding ECG with low bpm. The bottom plot is of a higher bpm. The opening and closing of the mitral valve and the aorta valve are also plotted.*

The result for detecting valve events are shown in Figure 8.16 and Figure 8.17. Figure 8.16 displays when the opening and closing of the aortic valve and mitral valve in the non-adjusted angular variance curve. We see from the plots the opening and closing events for each cardiac cycle both for a low bpm recording at the right plot in Figure 8.16 and a high bpm recording in the left plot in Figure 8.16. It is very interesting to see how they occurs

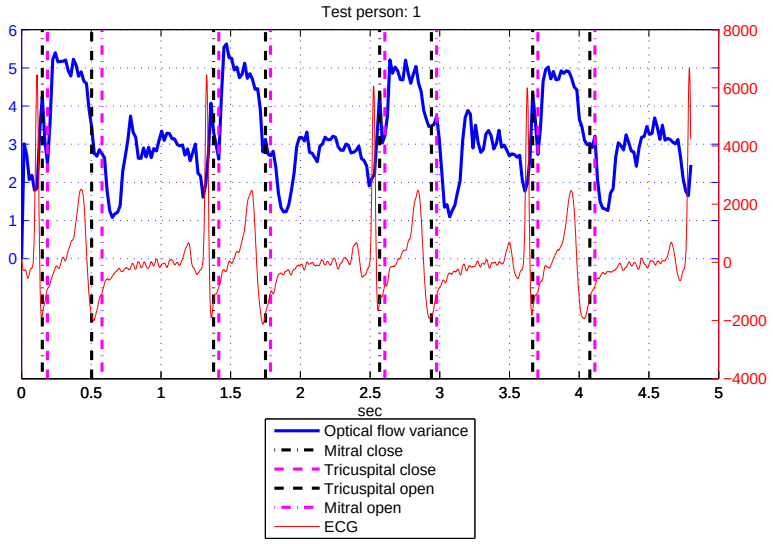

Figure 8.17: *The figure displays an apical four-chamber scan of low bpm with the mitral valve and tricuspid valve closing and opening marked.*

on the non-adjusted angular variance curve. When there are changes in the direction of the curve, different valves opens and closes. To better illustrate this, avi files were made. These are available at *folk.uio.no/jacobln*. We see that valve events repeat themselves at more or less the same points in the curve for each cardiac cycle. In Figure 8.17 we see how the mitral and tricuspid valve open and close in a low bpm recording. For each cardiac cycle both the opening and closing of the mitral and tricuspid valve occurs more or less at the same time and on the same events in the non-adjusted angular variance curve. It was not possible to show how these events would occur on the high bpm recording, because the scans were either of bad quality or not of the four chamber scan. This was the case for all the acquisitions on all the subjects. Form the interpretation of the different opening and closing events it looks like both for the apical long-axial and four-chamber scans the mitral valve close at the first little peak just before the maximum peak in each cycle and opens just after the the variance really have dropped from a high level on a little local peak. For the aortic valve in the apical long-axis scan it looks like it closes just before the variance really have increased, and opens when the variance drop as seen in Figure 8.16. For the four-chamber scan it looks more or less the same as for the aortic valve, only the mitral valve opens a bit later. Here it have to be taken to consideration that I am not an expert on studding ultrasound images and as mentioned earlier there has been no image processing on the .h5 images.

Chapter 9

Part II - Summary

9.1 Optical flow algorithm

Using optical flow to try to find the mechanical movements of the heart gave some very interesting results. The method seems to be quite robust because it showed good results when only one ROI was used even if the ultrasound recordings were of reduced quality. The optical flow method probably is best on acquisitions where no filtering for speckle or edges have been done and therefore using of the none processed data from .h5 files are believed be an advantage. The non-adjusted variance of angles curve also seems to have good features. This was seen both when we compared the curve with the ECG curve and when tested on the hearts valve events in a cardiac cycle.

Even though the results shown from the non-adjusted variance of angle curve looks promising as an alternative and supplement to the ECG curve, we have to be aware that the dataset it was tested on was small and the determination of the opening and closing events of the valves where done by a non-qualified person. (Me again:-))

Another ting to take into consideration is that all the acquisitions are apical scans. This implying that when we are looking at the optical flow from a specific angle, we will get a specific pattern, because the flow vectors are calculated on the basis of where the ultrasound probe is placed. I.e. on the front of the chest, parasternal, the non-adjusted variance of angles curve may not have have the same problem with wrapping and therefore might have different features. Then it can be possible to combine the mean and variance curve to make a curve with similar features. Since we do not have had any heart scan recordings other that apical scans we have not been able to verify this. We do believe that it will be possible to get a curve with a specific pattern for other type of scans than apical.

Chapter 10

General Discussion

10.1 Histogram-based methods vs optical flow

The mean pixel intensity curve used in Aase's algorithm was the basis and inspiration for looking at different methods that use the pixel intensities to find a repetitive pattern in ultrasound images. The histogram-based approach is based on the distribution of the pixel intensities in one frame or between two frames. Optical flow is based on the movement of structures between two frames. The choice of using dense optical flow was made because this method uses all the pixels from the image the same way as the histogram-based method does. The sparse optical flow method focuses on finding features in the image and tries to track these features throughout the recording. By selecting the dense method we do not need to choose which part of the heart that is contributing, and also capture these parts in all the recordings.

10.1.1 ROIs

In the histogram-based approaches we were eager to see how the different numbers of ROIs influenced the result. We saw that for a low bpm recording of the heart, for either one or several ROIs, most of the methods gave a repetitive pattern. This was also the result from using the optical flow method. For a high bpm recording all the histogram-based methods failed, whereas optical flow still managed to keep more or less the same pattern. It was interesting to see that using only one ROI in the optical flow algorithm gave the best result. The reason for this could be that when the image is divided into several ROIs, the ROIs that are homogeneous or have little variance will have small changes in information. This therefore makes it difficult to capture a good feature that varies over time. If we had managed to place the ROI over known events or features in the heart, it might have been possible to capture a better repetitive pattern on high bpm. The recording would also have been needed to be of higher quality, which is more difficult to

achieve when the heart is beating faster. Such an approach would probably require high quality recordings which is not always easy to achieve. To use the whole image as an input therefore seems to be a more robust approach. Dividing the image into many ROIs and only let a few go into the analysis approaches a sparse optical flow algorithm.

The results between two frames can not be equal for all datasets because the frame rate which the data was recorded at, was the same for both the high and low recording. This implies that the acquisition distance for a cardiac cycle is longer for higher heart rate than for a lower heart rate. If we were interested in tracking features or events locally in the heart the sparse optical flow method would have been a better approach.

10.1.2 Features in cardiac cycle curves

The curve received from using the non-adjusted angular variance in the optical flow method, shows a lot more features than any of the other curves found in the histogram-based methods. The ability to find features in the curve was something that we emphasized when looking at different methods to use because the features can be linked to events in the cardiac cycle, and also used as a tool when doing data processing on an ultrasound recording.

Chapter 11

Conclusion and further work

11.1 Conclusion

11.1.1 Cardiac cycle length estimation algorithm

The implementation of Aases cardiac cycle length algorithm showed that changing the similarity measure from SAD to correlation gave the same results in the estimation of the cardiac cycle length. The parameters used in Aase's algorithm seemed to be good choices after having tested different values, especially the differentiation of the mean pixel intensity curve gave a more robust algorithm. The adjustments suggested to make the cardiac cycle length algorithm boundary independent gave the correct result initially expected when tested on the ultrasound recording 55 bpm for a low recording and 102 bpm for a high recording.

11.1.2 Histogram-based similarity analysis

The use of histogram-based similarity analysis did not succeed in finding a pattern for both low and high bpm values. A simple pattern with a few features was found for the low bpm recording. For the high bpm recording it was difficult to find any specific pattern.

11.1.3 Optical flow

A repetitive pattern for both low and high pulse recording was found using the mean and variance of the length of the optical flow vectors. Nevertheless, what seemed to give the best repetitive pattern of the hearts cardiac cycle was using the variance of the angles of the optical flow vectors. The curve retrieved from the angle variance seemed to have features that could be linked to the ECG curve. From the angle variance curve it also looked like it could be possible to estimate/find the different valve events in the heart.

If the algorithms derived in this thesis had been tested on a larger number of datasets, the robustness of the algorithms had been shown which would have made it easier to draw stronger conclusions about the results.

11.2 Further work

As mentioned earlier the heart movement detection algorithm should be tested on a large number of recordings to verify how robust it is. Data from both healthy subjects and subjects with various heart diseases should be included to test the ability to detect features that are exclusive to certain conditions. Another application of this new algorithm could be to see if it was possible, during prenatal ultrasound scans, to detect the heart movement of the fetus.

It would also be interesting to see if it is possible to use the optical flow signature for stitching together images. All the scans done in this thesis have been apical scans and should be compared with the results from applying the algorithm to data from scans done from other angles. The optical flow algorithm was used on the .h5 formatted data which as mentioned before is an acquisition with no initial image processing or filtering that would remove speckle and enhance edges. Further work with this could be:

- See how the signatures would be affected if we applied the optical flow algorithm to the filtered data.
- The method used to find the flow for all pixels in a window was the dense method, and therefore look at the comparison between the dense and sparse method.
- See if it would be better to only track a few explicit features in the image.
- See if it could be possible to link the angle variance curve to heart diseases.
- Study in more detail the mean and variance of the optical flow length to see if this feature will give different information than the non-adjusted angular variance.

Appendix A

Appendix

A.1 Tables

	Recording 1				Recording 2				Recording 3				Recording 4			
	DR		NDR		DR		NDR		DR		NDR		DR		NDR	
Smooth	SCR	Bpm	SCR	Bpm	SCR	Bpm	SCR	Bpm	SCR	Bpm	SCR	Bpm	SCR	Bpm	SCR	Bpm
1	9	55	7	55	9	56	8	56	8	101	1	81	3	83	5	59
5	9	55	7	55	9	56	8	56	8	98	1	81	3	88	5	59
10	9	55	7	55	9	56	6	56	8	95	1	65	2	88	6	59
20	8	55	6	55	7	57	6	56	8	95	2	74	3	85	6	59

	Recording 1				Recording 2				Recording 3				Recording 4			
	DR		NDR		DR		NDR		DR		NDR		DR		NDR	
Smooth	SCR	Bpm	SCR	Bpm	SCR	Bpm	SCR	Bpm	SCR	Bpm	SCR	Bpm	SCR	Bpm	SCR	Bpm
1	9	55	8	54	9	56	9	56	8	101	7	98	3	79	2	83
5	9	56	8	54	9	56	9	56	8	98	7	98	3	79	2	83
10	9	55	8	54	9	56	8	56	7	98	7	95	2	77	2	83
20	9	55	7	54	9	56	6	56	9	95	3	88	1	76	3	83

Table A.1: *This table is of the correlation algorithm computed over 9 sector/masks. The correlation algorithm is computed over with different smoothing length and with(DR) or without (NDR) derived curve influenced if we use a long smoothing filter and what happens when the curve is derived (DR) and not derived(NDR). The computation is used on a dataset of length T=2. The table displays how many sectors (SCR) that will be in the confidence interval and the calculated bpm.*

A.2 Protocol

	Recording 1				Recording 2				Recording 3				Recording 4			
	DR		NDR		DR		NDR		DR		NDR		DR		NDR	
Smooth	SCR	Bpm	SCR	Bpm	SCR	Bpm	SCR	Bpm	SCR	Bpm	SCR	Bpm	SCR	Bpm	SCR	Bpm
1	20	55	14	55	20	56	15	56	12	102	7	107	3	76	12	69
5	20	55	14	55	20	56	16	57	12	102	3	88	4	79	12	69
10	19	55	13	55	20	56	14	57	11	104	0	75	2	74	11	61
20	18	55	13	56	20	56	9	57	7	107	2	64	3	76	13	67

	Recording 1				Recording 2				Recording 3				Recording 4			
	DR		NDR		DR		NDR		DR		NDR		DR		NDR	
Smooth	SCR	Bpm	SCR	Bpm	SCR	Bpm	SCR	Bpm	SCR	Bpm	SCR	Bpm	SCR	Bpm	SCR	Bpm
1	20	55	16	55	19	56	19	55	12	101	12	104	3	72	4	76
5	20	55	16	55	20	56	19	56	13	101	10	104	3	73	4	76
10	19	55	14	54	20	56	18	57	13	101	8	99	3	78	7	106
20	19	55	12	54	20	56	12	58	12	104	0	80	4	78	4	80

Table A.2: *This table is of the correlation algorithm computed over 20 sector/masks. The correlation algorithm is computed over with different smoothing length and with(DR) or without (NDR) derived curve influenced if we use a long smoothing filter and what happens when the curve is derived (DR) and not derived(NDR). The computation is used on a dataset of length T=2. The table displays how many sectors (SCR) that will be in the confidence interval and the calculated bpm.*

	Recording 1				Recording 2				Recording 3				Recording 4			
	DR		NDR		DR		NDR		DR		NDR		DR		NDR	
Smooth	SCR	Bpm	SCR	Bpm	SCR	Bpm	SCR	Bpm	SCR	Bpm	SCR	Bpm	SCR	Bpm	SCR	Bpm
1	45	55	36	56	46	56	37	57	30	101	17	101	14	101	11	98
5	46	55	36	56	47	56	37	56	29	101	16	101	15	101	11	95
10	46	55	35	56	44	56	33	57	30	101	14	101	14	104	10	95
20	45	55	29	56	37	57	26	56	23	101	9	104	16	101	10	90

	Recording 1				Recording 2				Recording 3				Recording 4			
	DR		NDR		DR		NDR		DR		NDR		DR		NDR	
Smooth	SCR	Bpm	SCR	Bpm	SCR	Bpm	SCR	Bpm	SCR	Bpm	SCR	Bpm	SCR	Bpm	SCR	Bpm
1	46	55	41	55	48	56	40	57	31	101	33	101	17	104	14	101
5	47	55	41	55	48	56	41	57	31	101	32	101	16	101	14	104
10	46	55	41	55	46	56	34	57	31	101	29	101	15	101	15	104
20	44	55	37	55	45	57	29	58	26	101	22	101	21	101	10	104

Table A.3: *This table is of the correlation algorithm computed over 49 sector/masks. The correlation algorithm is computed over with different smoothing length and with(DR) or without (NDR) derived curve influenced if we use a long smoothing filter and what happens when the curve is derived (DR) and not derived(NDR). The computation is used on a dataset of length T=2. The table displays how many sectors (SCR) that will be in the confidence interval and the calculated bpm.*

	Recording 1				Recording 2				Recording 3				Recording 4			
	DR		NDR		DR		NDR		DR		NDR		DR		NDR	
Smooth	SCR	Bpm	SCR	Bpm	SCR	Bpm	SCR	Bpm	SCR	Bpm	SCR	Bpm	SCR	Bpm	SCR	Bpm
1	80	55	71	56	79	56	66	57	51	101	29	104	36	98	13	94
5	85	55	69	56	88	56	65	57	54	101	30	104	29	98	18	95
10	83	55	66	56	87	56	64	58	59	101	29	104	28	98	14	90
20	76	55	47	57	75	57	47	57	41	104	18	107	22	98	19	85

	Recording 1				Recording 2				Recording 3				Recording 4			
	DR		NDR		DR		NDR		DR		NDR		DR		NDR	
Smooth	SCR	Bpm	SCR	Bpm	SCR	Bpm	SCR	Bpm	SCR	Bpm	SCR	Bpm	SCR	Bpm	SCR	Bpm
1	90	55	77	55	87	56	40	79	61	101	51	101	27	101	30	101
5	95	55	78	55	91	56	77	57	57	101	53	101	19	99	23	102
10	93	55	76	55	89	56	73	57	56	101	44	102	26	98	24	104
20	85	56	63	54	90	57	58	58	36	101	32	102	30	101	19	101

Table A.4: *The upper table shows the SAD algorithm for 100 masks. The lower table displays the Correlation algorithm. The algorithms are computed with different smoothing length and with(DR) or without (NDR) derivation. The computation is used on a dataset of length T=2. and length T=1.2 depending on the length of the dataset. The table displays how many sectors (SCR) that will be in the confidence interval and the calculated bpm.*

Antall test personer: 5-6 stk

Test apparat:

Famerate:

Protokoll Ultralyd opptak

Innstillinger:

- Opptaket skal gjøres som multiframe
- Data skal lagres som Raw dicom
- Frameraten skal være den samme på alle opptakene
- Opptaket skal gjøres i 2D
- EKG skal lagres
- Utskriftsformat skal ha ekg under ultralyd og øverste del av sektor skal være ca 3 cm ned på skjermen.

Hvordan skal opptaket utføres:

- Hvert opptak skal ha > 4 sykluser
- Skal gjøres 2 typer opptak
  1. 4 kammer snitt
  2. Long apical data snitt

- Testen skal gjennomføres med 2 forskjellige hjertefrekvenser:
  1. Hvilepuls → testperson ligger rolig på benken
  2. Høy puls → testperson utfører spensthopp i 1 min, ca 30 stk. Og legger seg på benken.
     - Har pulsen sunket mer enn 20 % før må det utføre punkt 2 repeteres.

References

S.A. Aase, S.R. Snare, H. Dalen, A. Støylen, F. Orderud, and H. Torp. Echocardiography without electrocardiogram. *European Journal of Echocardiography*, 12(1):3–10, 2011.

L.P. Badano, R.M. Lang, and J.L. Zamorano. *Textbook of Real-time Three Dimensional Echocardiography*. Springer London, Limited, 2011. ISBN 9781849964951. URL `http://books.google.no/books?id=FkQ3o\_x627UC`.

A. Berge. `http://www.uio.no/studier/emner/~matnat/ifi/INF5300/v13/~undervisningsmateriale/~inf5300_v2013_lecture3_motion_2pp.pdf`, 2013. Online; accessed May-2013.

G. Bradski. The OpenCV Library. *Dr. Dobb's Journal of Software Tools*, 2000.

L. G. Brown. A survey of image registration techniques. *ACM computing surveys (CSUR)*, 24(4):325–376, 1992.

E.J. Candes and T. Tao. Decoding by linear programming. *Information Theory, IEEE Transactions on*, 51(12):4203–4215, 2005. ISSN 0018-9448. doi: 10.1109/TIT.2005.858979.

T. M. Cover and J. A. Thomas. *Elements of information theory*. Wiley-Interscience, New York, NY, USA, 1991. ISBN 0-471-06259-6. URL `http://portal.acm.org/citation.cfm?id=129837`.

A.L. Edwards. *An Introduction to Linear Regression and Correlation*. Series of Books in Psychology. W. H. Freeman, 1976. ISBN 9780716705611.

G. Farnebäck. *Polynomial expansion for orientation and motion estimation*. PhD thesis, Linköping UniversityLinköping University, Computer Vision, The Institute of Technology, 2002.

M. Fatemi and A.C. Kak. Ultrasonic b-scan imaging: Theory of image formation and a technique for restoration. *Ultrasonic Imaging*, 2(1):1 – 47, 1980. ISSN 0161-7346. doi: 10.1016/0161-7346(80)90201-1. URL `http://www.sciencedirect.com/science/article/pii/0161734680902011`.

WSP Fernando, L. Udawatta, and P. Pathirana. Identification of moving obstacles with pyramidal lucas kanade optical flow and k means clustering. In *Information and Automation for Sustainability, 2007. ICIAFS 2007. Third International Conference on*, pages 111–117. IEEE, 2007.

J. M. Fitzpatrick, D. LG Hill, and C. R Maurer Jr. Image registration. *Handbook of medical imaging*, 2:447–513, 2000.

R. C. Gonzalez and R. E. Woods. *Digital Image Processing*. Pearson Education, Inc., 2008.

J. R. Hampton. *The E. C. G. made easy [by] John R. Hampton*. Churchill Livingstone, [Represented by Longman, New York] Edinburgh,, 1973. ISBN 0443010366.

Ge Healthcare. `http://www3.gehealthcare.com/en/Products/Categories/Ultrasound/Vivid/Vivid_E9`, 2013. [Online; accessed 13-June-2013].

D H. Johnson and D E. Dudgeon. *Array Signal Processing: Concepts and Techniques*. Simon & Schuster, 1992. ISBN 0130485136.

M.A. Lediju, M.J. Pihl, S.J. Hsu, J.J. Dahl, C.M. Gallippi, and G.E. Trahey. Magnitude, origins, and reduction of abdominal ultrasonic clutter. *Ultrasonics Symposium, 2008. IUS 2008. IEEE*, pages 50–53, 2008. doi: 10.1109/ULTSYM.2008.0013.

C-H Lin, C-M Weng, and Y-N Sun. Ultrasound image compounding based on motion compensation. In *Engineering in Medicine and Biology Society, 2005. IEEE-EMBS 2005. 27th Annual International Conference of the*, pages 6445–6448, 2005. doi: 10.1109/IEMBS.2005.1615974.

B.D. Lucas. *Generalized Image Matching by the Method of Differences*. Research Papers. Carnegie-Mellon University, Department of Computer Science, 1985.

J. B. A. Maintz and M. A. Viergever. A survey of medical image registration. *Med. Image Anal.*, 2:1?36, 1998.

MathWorks. `http://www.mathworks.se/`, 2013. [Online; accessed 13-June-2013].

NationalInstruments. `http://www.ssb.no/dodsarak`, 2013. [Online; accessed 12-February-2013].

D Patel and S Upadhyay. Article: Optical flow measurement using lucas kanade method. *International Journal of Computer Applications*, 61(10): 6–10, January 2013a. Published by Foundation of Computer Science, New York, USA.

D. Patel and S. Upadhyay. Optical flow measurement using lucas kanade method. *International Journal of Computer Applications*, 61(10):6–10, January 2013b.

J. Pope. *Medical Physics: Imaging*. Heinemann advanced science. Heinemann, 1999. ISBN 9780435570941. URL `http://books.google.no/books?id=xfbKH9epiZgC`.

StatisticsNorway. `http://www.ssb.no/dodsarsak`, 2011. [Online; accessed 12-February-2013].

A. Stoylen. Basic ultrasound, echocardiography and doppler for clinicans. `http://folk.ntnu.no/stoylen/strainrate/Ultrasound/`, April 2013.

B. B. Tempkin and W. C. Leonhardt. *Ultrasound scanning: principles and protocols*. Elsevier Saunders, 2009.

J. Vahrenhold. *Experimental Algorithms: 8th International Symposium SEA 2009, Dortmund, Germany, June 4-6, 2009, Proceedings*, volume 5526. Springer, 2009.

Wikipedia. `http://upload.wikimedia.org/wikipedia/commons/f/fa/Diagram_of_the_human_heart.svg`, 2013a. [Online; accessed 28-Januar-2013].

Wikipedia. `http://faculty.stcc.edu/AandP/AP/imagesAP2/heart/heartcond.jpg`, 2013b. [Online; accessed 28-Januar-2013].

Wikipedia. `http://commons.wikimedia.org/wiki/File:Wiggers_Diagram.svg#file`, 2013c. [Online; accessed 29-June-2013].